Published in final edited form as:

Nature. 2016 September 01; 537(7618): 112–116. doi:10.1038/nature19327.

Small molecule stabilization of the KSR inactive state antagonizes oncogenic Ras signalling

Neil S. Dhawan[1,2,*], **Alex P. scopton**[1,2,*], and **Arvin C. Dar**[1,2]

[1]Department of Oncological Sciences, The Tisch Cancer Institute, The Icahn School of Medicine at Mount Sinai, New York, New York 10029, USA

[2]Department of Structural and Chemical Biology, The Tisch Cancer Institute, The Icahn School of Medicine at Mount Sinai, New York, New York 10029, USA

Abstract

Deregulation of the Ras–mitogen activated protein kinase (MAPK) pathway is an early event in many different cancers and a key driver of resistance to targeted therapies[1]. Sustained signalling through this pathway is caused most often by mutations in K-Ras, which biochemically favours the stabilization of active RAF signalling complexes[2]. Kinase suppressor of Ras (KSR) is a MAPK scaffold[3–5] that is subject to allosteric regulation through dimerization with RAF[6,7]. Direct targeting of KSR could have important therapeutic implications for cancer; however, testing this hypothesis has been difficult owing to a lack of small-molecule antagonists of KSR function. Guided by KSR mutations that selectively suppress oncogenic, but not wild-type, Ras signalling, we developed a class of compounds that stabilize a previously unrecognized inactive state of KSR. These compounds, exemplified by APS-2-79, modulate KSR-dependent MAPK signalling by antagonizing RAF heterodimerization as well as the conformational changes required for phosphorylation and activation of KSR-bound MEK (mitogen-activated protein kinase kinase). Furthermore, APS-2-79 increased the potency of several MEK inhibitors specifically within Ras-mutant cell lines by antagonizing release of negative feedback signalling, demonstrating the potential of targeting KSR to improve the efficacy of current MAPK inhibitors. These results reveal conformational switching in KSR as a druggable regulator of oncogenic Ras, and further suggest co-targeting of enzymatic and scaffolding activities within Ras–MAPK signalling complexes as a therapeutic strategy for overcoming Ras-driven cancers.

Correspondence and requests for materials should be addressed to A.C.D. (arvin.dar@mssm.edu).

*These authors contributed equally to this work.

Author Information Coordinates and structure factors have been deposited with the Protein Data Bank under accession code 5KKR.

The authors declare competing financial interests: details are available in the online version of the paper. Readers are welcome to comment on the online version of the paper.

Author Contributions N.S.D. conducted biochemical, structural, and cell-line studies. A.P.S. synthesized compounds. A.C.D. supervised research. All authors analysed data.

Reviewer Information *Nature* thanks G. Bollag and the other anonymous reviewer(s) for their contribution to the peer review of this work.

Ras is the most frequently mutated human oncogene. Yet, despite recent breakthroughs, therapeutic options to target Ras-dependent cancers remain limited[1]. Studies conducted in several different model systems support the possibility of Ras-targeted interventions via KSR[3–5,8–10]. However, due to its status as a pseudokinase and role as a non-catalytic regulator of core signalling enzymes[11–13], pharmacological approaches that target KSR have been lacking. This is in contrast to current drug discovery and development efforts that have focused extensively on direct inhibitors of the Ras effector kinases RAF, MEK, and ERK[14].

To explore an alternative form of pharmacological modulation and identify Ras–MAPK antagonists via KSR, we focused on large forward genetic screens conducted in flies and worms that identified mutant Ras-selective suppressor alleles in KSR[3–5]. The studies in flies alone eval uated approximately 900,000 randomly mutated strains searching for genetic modifiers of a Ras(G12V)-dependent rough-eye phenotype[15]. We mapped the suppressor alleles onto the primary sequence of KSR (Extended Data Fig. 1a) and a recently determined X-ray crystal structure of the human KSR2 pseudokinase domain in complex with MEK1 and ATP, and noted a high concentration of suppressor mutations immediately adjacent to the KSR ATP-binding pocket (Fig. 1a). On the basis of this analysis, we hypothesized that the RAF and MEK interaction interfaces in KSR may be uncoupled through ligands that engage the KSR ATP-binding pocket. Specifically, we speculated that small molecules, which bias KSR towards a state similar to that revealed in the KSR2–MEK1–ATP crystal structure, might function as antagonists of KSR-dependent regulation of RAF and MEK.

To identify active-site-directed ligands of KSR, we screened a collection of 176 structurally diverse kinase inhibitors for direct competition of an activity-based probe (ATP^{biotin}) that specifically labels the ATP-binding pocket of purified KSR2–MEK1 complexes (Fig. 1b, c). From this analysis we identified APS-1-68-2 as a competitor of probe-labelling of KSR2–MEK1. This quinazoline–biphenyl ether compound has previously been described as both a Src and epidermal growth factor receptor (EGFR) family kinase inhibitor. Synthetic tailoring of APS-1-68-2 generated highly informative structure–activity relationships (Fig. 1d). For example, deletion of the terminal phenyl group (APS-1-82-1) or extension of the ether linker (APS-2-12) diminished KSR2–MEK1 probe competition. Notably, addition of a single methyl group at the internal phenyl generated a potent probe compound (APS-2-79; IC_{50} of KSR2 = 120 ± 23 nM), whereas the similar dimethyl substituted com pound (APS-3-77) was essentially inactive (IC_{50} of KSR2 > 10,000 nM).

To assess the biological function of these compounds as Ras–MAPK pathway antagonists, we developed a simplified cell-based reconstitution system to directly monitor KSR-driven MAPK signalling (Fig. 1e). This system, in which cellular MAPK signalling is dependent on KSR expression, was found to be sensitive to known Ras suppressor mutations in KSR (Fig. 1f). Likewise, APS-2-79 also suppressed KSR-stimulated MEK and ERK phosphorylation (Fig. 1g; $P < 0.005$ lanes 1 versus 2). The suppression of MAPK signalling by APS-2-79 was dependent on direct targeting of KSR as an active site mutant (KSR(A690F)), which has previously been demonstrated to stimulate KSR-based MAPK outputs independent of ATP-binding[16], significantly diminished the activity of APS-2-79 (Fig. 1g; lanes 5 versus 6, NS; lanes 2 versus 6, $P < 0.005$). Notably, the negative control for KSR-binding (analogue APS-3-77; see Extended Data Fig. 2b, c for comparative selectivity profiling) was inactive,

whereas a positive-control RAF inhibitor, dabrafenib, was active irrespective of the KSR-mutational status (Fig. 1g). Therefore, on the basis of similarity in phenotype and also direct-binding activity, we identify APS-2-79 as a small-molecule mimic of KSR alleles that suppress oncogenic Ras mutations.

KSR-based activity of APS-2-79 as a MAPK antagonist was further evaluated using reconstitution assays. Dose-dependent phosphorylation of MEK on Ser218/Ser222 by RAF *in vitro* could be enhanced at least fivefold in the presence of KSR (Extended Data Fig. 3a–c). KSR-stimulated MEK phosphorylation by RAF was markedly reduced by the addition of APS-2-79, but not by APS-3-77 (Extended Data Fig. 3d, e). APS-2-79 was inactive when KSR was absent or when the KSR2(A690F) mutant was used for *in vitro* assays (Extended Data Fig. 3d, f, g), suggesting that the activity of APS-2-79 derives from direct targeting of KSR. Indeed, APS-2-79 lacked direct activity against the highly homologous active RAF family kinases, including recombinant BRAF and CRAF, or cellular BRAF(V600E) (Extended Data Figs 2, 3, 4a). Therefore, on the basis of reconstitution and selectivity assays, we conclude that APS-2-79 functions as an antagonist of MEK phosphorylation by RAF through direct binding of the KSR active site.

Notably, we found that a previously described ATP-competitive and active-state binder of KSR termed ASC24 (ref 7), in contrast to APS-2-79, did not antagonize KSR-dependent MEK phosphorylation by RAF (Extended Data Fig. 3d, e), suggesting that inhibition of catalytic activity alone in KSR is insufficient to block MAPK signalling. Consistent with this notion, removal of putative KSR phosphorylation sites[7] in MEK neither impeded MAPK signalling nor blocked the inhibitory activity of APS-2-79 within cells (Extended Data Fig. 4b).

Previous studies established that genetic suppressors in KSR may impede RAF-induced conformational changes in KSR required for MEK activation or destabilize KSR–MEK and KSR–RAF complexes[6,7,12,17–19]. To distinguish between such possible modes of action, we determined an X-ray crystal structure of the KSR2–MEK1 complex bound to APS-2-79 (Fig. 2a). In the APS-2-79-bound state, KSR2 binds MEK1 in a 1:1 fashion within a quaternary arrangement that is nearly identical to the ATP-bound state of KSR2–MEK1 complexes[7] (Extended Data Fig. 5). Within both states, KSR2 and MEK1 bind via a face-to-face arrangement mediated largely through reciprocal helix αG and activation segment interactions, and KSR2 homodimerizes through the N-lobe along a crystallographic two-fold symmetry axis producing a hetero-tetramer of KSR2–MEK1 dimers.

In the APS-2-79-bound state, only KSR2 was found to possess strong electron density that could be assigned to APS-2-79 (Extended Data Fig. 6a, b). Two portions of APS-2-79 engage distinct regions in KSR2. First, the biphenyl ether extends to a sub-pocket within KSR2, defined by Thr739, Arg692, Asp803 and a hydrophobic shell composed of Phe725, Tyr714 and Phe804 (Fig. 2b, c). Stacking interactions between the terminal phenyl in APS-2-79, and Phe725, Tyr714 and Phe804 in particular are expected to provide strong interactions between KSR2 and APS-2-79 through the arrangement of a four-member aromatic-pair network (Fig. 2b, c). The existence of this network was substantiated by removal of the terminal phenyl in APS-2-79-like compounds, which greatly diminished

competition of ATP^{biotin} probe-labelling in KSR2 (Extended Data Fig. 7; APS-1-68-2 versus APS-1-70-1 and APS-1-82-1). This network of aromatic-pair interactions, in addition to other amino acid substitutions, probably contributes to the selectivity of APS-2-79 for KSR over RAF (Extended Data Fig. 6c, e). Second, a hydrogen bond between the N1 in the quinazoline core of APS-2-79 and the backbone at Cys742 further mediates APS-2-79–KSR2 interactions. Notably, functionalization of the N1 with a methyl group (APS-3-6) greatly diminished KSR2–MEK1 activity, whereas replacement of the N3 with –CH (APS-2-16) was moderately tolerated (Extended Data Fig. 7). Therefore, on the basis of crystallographic analysis and also structurE–activity relationships data from our analogue series, APS-2-79 binds directly to KSR2 within the KSR2–MEK1 complex.

In both the APS-2-79- and ATP-bound states of KSR2–MEK1, KSR2 directly engages the activation segment of MEK1, burying the Ser218–Ser222 region and presumably shielding this segment of MEK from promiscuous phosphorylation. The KSR2–MEK1–APS-2-79 structure revealed a portion of KSR2 that was not previously modelled in the ATP-bound complex (Extended Data Fig. 6d). This region, encompassing residues Ile809 to Gln814, which we refer to as the induced lock, forms an extension of the activation segment C terminus to the conserved DFG motif, and forms an anti-parallel β-strand with the peptide sequence centred around Arg823 in KSR2 (Fig. 2d). Additionally, the ordering of residues Ile809 to Gln814 in KSR2 occurs at the expense of disorder of residues 674 to 676 in the P-loop, which in the ATP-bound state directly coordinates the β and γ phosphates (Fig. 2e). The two modes by which ATP and APS-2-79 affect KSR-based interactions on MEK appear mutually exclusive as both ligands induce conformations that would otherwise clash with one another (Fig. 2e). We interpret these structures to suggest that APS-2-79 stabilizes an inactive state of KSR2 characterized by reinforcement of negative regulatory inter actions. Indeed, APS-2-79 behaves as a KSR-dependent antagonist of RAF-mediated MEK phosphorylation by shifting the equilibrium of KSR–MEK complexes so as to populate the OFF state (Extended Data Fig. 5c).

Comparison of the ATP-bound and APS-2-79-bound states of KSR2–MEK1 suggested that APS-2-79 antagonizes RAF phosphorylation on MEK indirectly by impeding KSR–RAF heterodimers. As well as APS-2-79 binding, the dimer interface of KSR2, including residues Trp685 and His686, demonstrated perturbations relative to the ATP-bound conformation (Fig. 3a, Extended Data Fig. 8). To investigate directly the effect of APS-2-79 on KSR2–BRAF dimerization, we used bio-layer inferometry (BLI) to monitor real-time association and dissociation of KSR2–MEK1 or free MEK1 to a sensor tethered with immobilized BRAF. In control experiments, we found that KSR2–MEK1 complexes did not associate with immobilized BRAF in a 1:1 fashion (Fig. 3b), probably owing to the formation of higher order BRAF–KSR2–MEK1 complexes. In contrast, BRAF bound to free MEK1 in a 1:1 fashion with a dissociation constant (K_d) = 51 ± 3.8 nM (Fig. 3c), which is in close agreement to published work[20].

To specifically monitor KSR2–BRAF dimerization relative to other possible interactions, we identified a mutation in BRAF(F667E) that eliminates binding to free MEK but not KSR2–MEK1 complexes (Fig. 3d, e). KSR2–MEK1 interacted in a 1:1 fashion with the BRAF(F667E) mutant with a K_d of 1.99 ± 0.09 μM; closely matching previously published

BRAF–BRAF dimerization values[6]. Notably, the addition of a secondary mutation, known to perturb KSR2–BRAF dimers (BRAF(F667E/R509H); Fig. 3f), completely abrogated any binding signal between KSR2–MEK1 and BRAF. In the presence of APS-2-79, the KSR2–BRAF(F667E) dimers did not associate (Fig. 3g), consistent with the prediction of the crystal structure suggesting that APS-2-79 may impede RAF–KSR dimers. In contrast, the control com pound APS-3-77 did not impede KSR2–BRAF interactions (Extended Data Fig. 8c). Therefore, we conclude that BRAF can dimerize with KSR2–MEK1 complexes directly via KSR2, and this interaction is antagonized by APS-2-79.

Ras mutations occur in approximately 25% of all cancer patients and are highly associated with poor response to therapy[1]. Significant progress has been made in targeting BRAF(V600E)-mutant melanoma, however RAF and MEK inhibitors have failed to achieve significant clinical efficacy in Ras-mutant disease owing in part to mechanisms of inhibitor-induced transactivation and feedback, respectively[21]. MEK-inhibitor feedback has been characterized by upstream Ras activation and induction of higher-order RAF–RAF and also RAF–KSR complexes[22–24]. In an engineered cell system, we found that a Ras-suppressor allele (R718H[6,7]) within KSR reduced MEK inhibitor-induced feedback (Extended Data Fig. 4c), suggesting the possibility that KSR heterodimerization may limit the efficacy of MEK inhibitors. Owing to the more pronounced role of KSR in Ras-mutant, as opposed to RAF-mutant signalling[15,25], and the ability of APS-2-79 to impede KSR–RAF heterodimerization, we hypothesized that stabilization of the KSR-inactive state (KSRi) via APS-2-79 may potentiate the effect of MEK inhibitors by limiting feedback in Ras-mutant models. We therefore tested for synergy of APS-2-79 with MEK inhibitors in Ras-mutant cell lines, and used RAF-mutant cell lines as controls.

We found that APS-2-79 shifted the cell viability dose response to trametinib in Ras-mutant cell lines HCT-116 and A549, but not BRAF mutant cell lines SK-MEL-239 and A375 (Fig. 4a). Although the cellular effects of APS-2-79 alone were modest, combination analysis over full concentration matrices revealed that KSRi synergizes with trametinib, and other MEK inhibitors (Extended Data Fig. 9a), specifically in KRAS mutant cell lines (Fig. 4b). APS-3-77, and additional control compounds (Extended Data Fig. 9b and 10), did not demonstrate Ras-mutant-specific synergy, supporting the hypothesis that the enhanced activity of trametinib when combined with APS-2-79 depends on co-modulation of KSR. To determine the possible mechanism for APS-2-79 and trametinib synergy, we examined MAPK signal ling and found that APS-2-79 treatment caused a twofold enhancement in the IC_{90} of trametinib on ERK phosphorylation in the Ras-mutant HCT-116 cell line but not the RAF-mutant SK-MEL-239 cell line (Fig. 4c, Extended Data Fig. 4d). The data presented here provide proof-of-concept for the use of KSRi to overcome a key liability of a clinical MEK inhibitor in K-Ras mutant cells. Indeed, we posit stabilization of the KSRi as a mechanism to impede feedback activated Ras–MAPK signalling induced by MEK inhibition (Fig. 4d).

Here we have identified a unique conformation in KSR through the discovery of APS-2-79. This compound offers a foundation for the development of a new class of targeted therapies based on stabilization of the KSR inactive state. Future efforts will be directed towards improving the pharmacological properties of APS-2-79 to enable *in vivo* and clinical studies.

In general, the stabilization of conformational states with small-molecule modulators may be an effective strategy to target other pseudokinases[26,27]. Furthermore, the results presented here, using KSRi in combination with clinical MEK inhibitors, suggests a mechanism to improve the efficacy of inhibitors that target enzymatically active kinases through co-modulation of pseudokinase–active kinase signalling complexes.

Full Methods

Expression and Protein Purification of KSR2(KD):MEK1

Codon optimized versions of human KSR2 kinase domain (KSR2(KD)), residues 634-950) and rabbit MEK1 (1-393) were co-expressed from the pFastbac dual vector (Thermo Fisher) using the baculovirus/SF21 insect cell system. Note: we refer to KSR2(KD):MEK1 and KSR2:MEK1 interchangeably throughout the manuscript unless otherwise noted. TEV-cleavable His_6 tags were added to the N-termini of both KSR2(KD) and MEK1. SF21 cells expressing the KSR2(KD):MEK1 complex were lysed by freeze-thaw and sonication. Cobalt resin (Clontech) was used to capture KSR2(KD):MEK1 complexes, and eluted proteins were subsequently dialyzed in 50 mMTris pH 7.5, 200 mMNaCl, 10mM $MnCl_2$, and 5 mM DTT to which TEV protease and λ-phosphatase were added. The dialysis buffer was also supplemented with protease inhibitor cocktail tablets (Thermo Fisher). Dialysis retentate was diluted 3 fold and applied to a 5 mL HiPrep SP HP column (GE Healthcare) from which excess MEK1, TEV, and the 1:1 KSR2:MEK1 complex were separated using a salt gradient (50 to 1000 mMNaCl)(Extended Data Fig. 1C). Fractions containing the 1:1 KSR2(KD):MEK1 complex were confirmed by gel electrophoresis and coomassie staining. Selected fractions were then pooled and applied to a Hiprep Superdex 200 10/300 GL size exclusion column for final purification in buffer consisting of 25mM Tris pH 7.5, 200 mM NaCl, and 10mM DTT. KSR2(KD):MEK1 eluted in two peaks, representing heterodimer (minor) and heterotetramer (major) species. Excess unphosphorylated MEK1, which was purified separately over a Hiprep Superdex 200 10/300 GL size exclusion column in buffer 25mM Tris pH 7.5, 200mM NaCl, and 10mM DTT eluted as a monomer. Expression and purification of the KSR2(KD^{A690F}):MEK1 (1-393) mutant and the crystallized KSR2(KD):MEK1(35-393) complexes were purified in the same fashion.

B-RAF and B-RAF mutant constructs (B-RAF(V600E), B-RAF(F667E), B-RAF (F667E-R509H)) were purified as previously described with slight modification[28]. In particular, we utilized a modified variant of B-RAF (I543A, I544S, I551K, Q562R, L588N, K630S, Y673S, A688R, L706S, Q709R, S713E, L716E, S720E, P722S, K723G) that could be expressed in high yield from *E.Coli* and which also retained near wild-type levels of B-RAF binding activity towards free MEK1. ERK2 was purified as previously described[29]. C-RAF was purchased from EMD Millipore (14-352). MEK-active, a pre-phosphorylated form of MEK, was also purchased from EMD Millipore (14-429).

ATP-biotin competition and reconstituted kinase assays

To identify active site directed ligands of KSR, we conducted competition experiments against an activity-based probe (ATP^{biotin}) that specifically labels the ATP-binding pocket of purified KSR2:MEK1 complexes (Fig. 1B). ATP^{biotin} transfers a desthio-biotin group via a

reactive acyl-phosphate linkage onto active-site lysines when bound to either KSR2 or MEK1 (Extended Data Fig. 1D; see ref.[30]). Competition experiments demonstrated that labeling occurs within the active sites of both KSR2 and MEK1 with free ATP IC_{50} values of 86 μM and 133 μM, respectively (Extended Data Fig. 1F). We also confirmed that this probe leads to a covalent attachment of desthiobiotin on KSR through detection with Streptavidin-HRP and intact mass spectrometry, the latter of which confirmed the addition of one or two desthiobiotin groups (equivalent to a mass increase of 196.1 Da per desthiobiotin group) onto both MEK1 and KSR2, respectively, under non-saturating conditions (Extended Data Fig. 1E). For intact masses, purified KSR2:MEK1 complexes were analyzed by liquid chromatography-tandem mass spectrometry (LC-MS) on a Waters Xevo TQD system through deconvolution of molecular ion peaks (MaxEnt; MassLynx).

KSR2 is highly unstable when expressed in isolation, and we therefore conducted all biochemical assays on purified KSR2:MEK1 complexes. The ATP based competition experiments suggested the utility of the ATP^{biotin} competition assay to identify direct binders of KSR2, MEK1, or both kinases within purified complexes. We screened a collection of 176 structurally diverse commercially available and in-house synthesized kinase inhibitors for direct competition of ATP^{biotin} probe labeling (Fig. 1C). ATP-biotin competition screens (as presented in Figure 1C) were performed by pre-incubating 0.5 μM of KSR2-MEK1 with 20 μM of compounds, 25 mMTris pH 7.5, 150 mMNaCl, 10 mM MgCl2, and 2% DMSO. ATP^{biotin} was then added to initiate labeling at a final concentration of 2 μM, and following 5 minutes of incubation, the reactions were quenched by addition of 6X SDS loading dye. Samples were applied to a 4–20% Tris-HCl gel, separated, and then transferred to a nitrocellulose membrane. The membrane was blocked with 5% bovine serum albumin diluted in TBS-T for 30 minutes and subsequently probed with the Pierce™ High Sensitivity Streptavidin-HRP overnight. For preliminary assays, compounds were screened at least twice at a concentration of 20μM. Western blot signals were visualized using enhanced chemiluminescence and a CCD based detector on a ChemDoc XRS+ imaging system (Biorad). Image acquisition and analysis, including quantification of band intensities, was performed using Image Lab™Software (Biorad).

To determine compound IC_{50} values against KSR2:MEK1, BRAF, BRAF(V600E), CRAF, MEK, and ERK, 50nM of protein was incubated with 8 doses of inhibitor from 78nM to 5μM in a two-fold dilution series. 2μM of ATP^{biotin} was added to initiate labeling, and incubated for 5 minutes before quenching with 6X SDS load dye. Reactions were resolved by gel electrophoresis and western blotting as described above. Assays were completed in duplicate and non-linear dose response curves were used to derive IC_{50} values using Prism 6.0 software (Graphpad). See Extended Data Fig. 2B and 7 for representative images of gels from which IC_{50} values were derived.

For the B-RAF and C-RAF phosphorylation assays (Extended Data Figure 3), the indicated concentrations of B-RAF or 5nM of C-RAF were pre-incubated with 500 nM KSR2:MEK1 or 500 nM MEK1. Compounds diluted in DMSO were added at a final concentration of 1 μM and incubated for an additional 15 minutes in buffer containing 25 mM Tris pH 7.5, 150 mM NaCl, 10 mM $MgCl_2$, and 2% DMSO. Kinase reactions were initiated by the addition of 1 mM ATP and halted at the indicated times by the addition of 6X SDS loading dye.

Samples were applied to 4-15% Tris-HCl gradient gels (Biorad) first and then transferred to nitrocellulose, blocked in 5% milk TBS-T, and then probed overnight with a MEK1/2 Ser218-Ser222 phospho-specific antibody (Cell Signaling) to determine RAF kinase activity. Chemiluminescence visualization and band quantification was performed as described above.

APS-2-79 and APS-3-77 were assayed against a panel of 246 kinases (ThermoFisher) to measure percentage inhibition values and derive kinome profiles (Extended Data 2C, D). Both compounds were screened at 1 μM and raw data is in Supplementary Table 1. Detailed procedures for kinase reactions and assay formats are described athttp://www.thermofisher.com/kinaseprofiling.

Crystallization of KSR2(KD):MEK1 complexed with APS-2-79

Prior to crystallization, the KSR2(KD):MEK1(35-393) complex was buffer exchanged via size exclusion chromatography in 15 mM Bis-Tris pH 6.5, 150 NaCl, 1 mM TCEP, and 5 mM DTT. The KSR2(KD):MEK1(35-393) complex was concentrated to 10 mg/ml and incubated with 500 μM APS-2-79. Aggregates were removed through centrifugation at 14,000 g for 10 minutes. Over a thousand crystallization conditions were tested using in-house and sparse matrix screens via hanging-drop methods at 4, 10, and 22 °C. Multiple conditions resulted in small and poorly diffracting crystals. Ultimately, relatively large hexagonal shaped crystals of approximately 200 microns in size arose from a condition containing 12% PEG-3350, 100 mM Bis-Tris pH 6.25, 200 mM sodium citrate, and 10 mM Magnesium Acetate. These crystals were flash-frozen following step-wise soaking in mother liquor spiked with increasing concentrations of ethylene glycol (25% maximum). A 3.5 Å data set was collected at the Advanced Photon Source on beamline 23-ID-B (Argonne National Laboratory). Diffraction images were indexed and scaled using XDS. The structure of KSR2(KD):MEK1 in complex with APS-2-79 was solved by molecular replacement using Phaser[31] based on searches of KSR2 (chain B) and MEK1 (chain C) models derived from the KSR2(KD):MEK1:ATP crystal structure (PDB code: 2Y4I). Model building was performed with Coot[32]. Rigid body and maximum likelihood based refinement protocols were implemented through Phenix[33]. APS-2-79 and induced-lock segments were omitted from early rounds of refinement. Crystals for the ATP and APS-2-79 bound KSR2:MEK1 complexes share similar unit cell dimensions, space group symmetry, and X-ray diffraction properties. Detailed data collection and refinement statistics are included in Supplementary Table 2.

Cell Culture, Plasmids, and Western Blotting

A375, HCT-116, LOVO, and A549 cells were obtained from the American Type Culture Collection. 293H, SK-MEL-239, COLO-205, SK-MEL-2, SW1417, SW620, MEWO, CALU-6 and H2087 cells were graciously provided by the Poulikakos Lab at the Icahn School of Medicine at Mount Sinai. HEPG2 cells were graciously provided by the Lujambio Lab at the Icahn School of Medicine at Mount Sinai. These lines tested negative for mycoplasma contamination. 293H, A375, HCT-116, A549, SK-MEL-2, SK-MEL-239, and HEPG2 cells were maintained in DMEM with 10% fetal bovine serum (FBS) supplemented with penicillin/streptomycin. COLO-205, SW1417, H2087 were maintained in RPMI with

10% FBS supplemented with penicillin/streptomycin. LOVO cells were maintained in DMEM/F12 with 10% FBS supplemented with penicillin/streptomycin.

All cell signaling assays (as shown in Figure 1E-G, 4, Extended Data Figure 4) were performed by plating 100K cells per well in a 12-well dish. Cells were plated 24 hours prior to transfection or inhibitor treatments. Cells were lysed and harvested in RIPA buffer supplemented with Halt phosphatase and protease inhibitor cocktail (Roche 78440). 6X SDS loading dye was added and samples were heated at 95°C for 5 minutes. Samples were run on 4-15% Tris-HCL gradient gels, transferred to nitrocellulose, and blocked for 1hr with 5% milk TBS-T. Blots were probed overnight with primary antibody in 5%BSA TBS-T.

Cell viability assays were performed in 96 well plates. Optimal cell densities for 96 well plate assays were determined to obtain linear growth over the time course of assays. Specifically, A549, HCT-116, A375, SK-MEL-239, COLO-205, LOVO, SK-MEL-2, CALU-6, MEWO, SW620 and SW1417 cells were plated at 500 cells per well and treated with inhibitors for 72hrs before measuring viability. H2087 and HEPG2 cells were plated at 2000 cells per well, and treated with inhibitors for 72hrs. Cell viability was measured using resazurin, and the percent cell viability was determined by normalizing inhibitor-treated samples to DMSO controls.

Antibodies for detection of KSR1 (Product number: 4640), FLAG (Product number: 8146), GFP (Product number: 2555), pMEK (Product number: 9121), pERK (Product number: 9101), pAMPK (Product number: 2531) and tMEK (Product number: 9122) were obtained from Cell Signaling. Western blotting was performed as described above. For primary antibody detection, blots were washed several times and probed for 1hr with anti-Mouse-HRP or anti-Rabbit-HRP (Cell Signaling) in 5% milk TBST.

KSR1-FLAG (Addgene ID:25970) and MEK1-GFP (Addgene ID:14746) plasmids were obtained from Addgene. B-RAF-V600E plasmids were graciously provided by the Poulikakos Lab. The plasmids for expression and purification of RAF constructs were generated by DNA 2.0. Constructs harboring mutations were generated by site-directed mutagenesis (Agilent). To normalize protein expression levels of different KSR constructs (Figure 1, Extended Data Figure 4), the following concentration of plasmid were transfected in 293H cells: KSR1(WT)-400ng, KSR1(A690F)-300ng, KSR(R718H)-700ng, KSR(C910Y)-3000ng, KSR(W884D)-3000ng, KSR(A736E)-700ng, KSR(A690T)-600ng, and KSR(MEK^{AAAA})-400ng. DNA transfections were carried out using Fugene 6 (Promega) in accordance with the manufacturer's recommendations.

Trametinib, Dabrafenib, PD0325901, AZD6244, Binimetinib, and SCH722984 were obtained from Selleck Chemicals. Wyeth-2b was obtained from Wellspring Biosciences. All compounds were dissolved in DMSO and subsequently diluted for biochemical and cellular experiments.

Synergy Analysis and Scoring

The Bliss score is defined as the difference between observed and predicted growth inhibition values for drug combinations within cancer cell lines[34]. Predicted combination

values are determined from the single agent dose responses of each compound, and Bliss scores were calculated by determining the difference between the expected combination value [Fractional response of Drug 1 (Fa) + Fractional effect of Drug 2 (Fb))-(Fa*Fb)] and the observed combination value (the viability observed from combination treatment with Drug1 and Drug2 normalized relative to DMSO controls). To determine if two drugs were synergistic (ie. in practice, where scores are significantly greater than 0), we analyzed the combinations (eg. Trametinib and APS-2-79) over a 10 × 5 matrix, and from this analysis calculated Bliss scores as the sum of differences between observed and predicted growth inhibition for each combination tested (as displayed in Figure 4 and Extended Data Figure 9; also Supplementary Table 4). Average Bliss scores and standard deviations were determined from two biological replicates of full matrices for each cell line and combination. Combination indexes (CI)[35] were separately calculated using the Compusyn Software developed by Combosyn Inc. In general, CIs less than zero are considered synergistic.

Biolayer Inferometry Using Octet Red 96

Interactions between purified B-RAF and the KSR2:MEK1 complex were measured using biolayer inferometry on the Octet Red96 system (Forte Bio). Binding experiments were performed at 30°C in buffer containing 10 mM phosphate-buffered saline pH 7.2, 1 % BSA, and 0.01% Tween. B-RAF and B-RAF mutant proteins were biotinylated using EZ-Link™ Sulfo-NHS-Biotinin buffer containing 10 mM phosphate-buffered saline pH 7.2 and 10% glycerol according to manufacturer instructions (Thermo Fisher, 21217). Excess biotin was removed overnight through dialysis and recaptured material was subsequently concentrated to 3 mg/mL and snap frozen prior to binding assays. For the studies described in Figure 3 and Extended Data Figure 8, 300 nM of biotinylated B-RAF was captured on pre-immobilized streptavidin Dip and Read sensor heads (ForteBio, 18-5019) with total B-RAF loaded up to a refractive index of between 1 and 1.5 nanometers. RAF-immobilized sensor heads were subsequently incubated in solutions containing increasing concentrations of purified KSR2:MEK1 or MEK1 (range: 625 nM to 10 μM in two-fold dilutions) and the association of these complexes was measured over 660 seconds. Dissociation was then monitored over 840 seconds in buffer solution. To measure the effects of compounds on KSR2:MEK1 or free MEK1 assembly with BRAF, all compounds were pre-incubated with KSR2:MEK1 or free MEK1 at a concentration of 25 μM. Data sets were normalized and analyzed using global fit binding models over all concentrations(Fortebio software) to derive K_{on}, K_{off} and K_D values as shown in Figure 3 and Extended Data Figure 8.

Chemical Synthesis

General Methods—All solvents were purchased from Sigma-Aldrich and were used as received; anhydrous solvents were used for reactions, and HPLC grade solvents were used for aqueous work ups, recrystallizations and chromatography. The palladium metal on solid support, used in hydrogenation reactions, was purchased from Sigma-Aldrich as 10% w/w on activated carbon (dry basis), with 50% w/w water added (Degussa type); designated in procedures as “5% w/w on activated carbon”. Other reagents were purchased from various vendors and were used as received. Reactions were run as described in the individual procedures using standard double manifold and syringe techniques. Glassware was dried by baking in an oven at 130 °C for ≥12h prior to use, or flame-dried. The pH of aqueous

solutions was estimated using pH paper. Vacuum filtrations were carried out using a house vacuum line (~100 torr). In the individual procedures, the phrases “concentrated under vacuum” and “concentrated to dryness” mean that solvent was removed on a rotary evaporator using a diaphragm pump (with an automatic vacuum regulator) and then remaining traces of volatiles were removed on a high-vacuum (<1 torr) oil pump. Unless specified otherwise, the term “flask” refers to the round-bottomed variety.

Reactions were monitored by TLC using EMD silica gel 60 F_{254} (250 μm) glass-backed plates (visualized by UV fluorescence quenching and stained with basic $KMnO_4$ solution) and by liquid chromatography-tandem mass spectrometry (LC-MS). Analysis by reverse-phase LC-MS was carried out on a Waters Aquity I-Class UPLC system, with a C18 column (2.1 × 30 mm, 1.7 μm particle size), heated at 50 °C, eluting at 0.6 mL/min, using a 3 min linear gradient method with a mobile phase consisting of water/acetonitrile (0.1% v/v formic acid added to each): 95:5→1:99(0-2.5 min), 1:99(2.5-3 min). Sample runs were monitored using alternating positive/negative electrospray ionization (50-1000 amu) and UV detection at 254 nm. Dimensions of “plugs”, “pads” and “columns” for filtration or flash chromatography are reported as: ((diameter × length) cm). The 5¾ inch pipets (4 mL) used for filtration and micro scale flash chromatography were purchased from Fisher Scientific (product number 22-378-893). Automated preparative normal- and reverse-phase chromatography was carried out on an Interchim PuriFlash 450 purification system with a diode array detector (runs were monitored at 220-400 nm) Pre-packed silica gel cartridges (12, 25 and 40 g) were employed for normal-phase chromatography, eluting at 20-30 mL/min. For reverse-phase chromatography a C18 column (30 × 150 mm, 5 μm particle size) was used, eluting at 15-20 mL/min with a pressure limit of 50 bar. ^{1}H NMR spectra were recorded at 400 MHz on a Bruker spectrometer and are reported in ppm using the residual solvent signal (dimethylsulfoxide-d_6 = 2.50 ppm) as an internal standard. Data are reported as: {(δ shift), [(s=singlet, d=doublet, dd=doublet of doublets, br=broad, m=multiplet), (*J*=coupling constant in Hz) and (integration}. Proton-decoupled ^{13}C NMR spectra were recorded at 100 MHz on a Bruker spectrometer and are reported in ppm using the residual solvent signal (dimethylsulfoxide-d_6 = 39.5 ppm) as an internal standard.

6,7-Dimethoxy-N-(4-phenoxyphenyl)quinazolin-4-amine hydrochloride (APS-1-68-2)—An 8 mL vial was charged with 4-chloro-6,7-dimethoxyquinazoline (56.2 mg, 0.250 mmol), 4-phenoxyaniline (55.6 mg, 0.300 mmol) and 2-PrOH (5 mL). The vial was sealed with a screw cap and the mixture was heated at 70-75 °C and stirred for 12h. After the reaction mixture had cooled to room temperature, the precipitate was collected by vacuum filtration (sintered glass funnel) and the solid was washed with 2-propanol (X2) and hexanes (X2). Air-drying yielded 101 mg (99%) of the title compound as a light-yellow solid: **^{1}H NMR** (400 MHz, DMSO-d_6) δ 14.91 (br s, 1H), 11.50 (br s, 1H), 8.80 (s, 1H), 8.37 (s, 1H), 7.70 (d, *J* = 8.9 Hz; 2H), 7.46-7.39 (m, 2H), 7.37 (s, 1H), 7.20-7.15 (m, 1H), 7.11 (d, *J* = 8.9 Hz; 2H), 7.09-7.04 (m, 2H), 4.02 (s, 3H), 3.99 (s, 3H); **^{13}C NMR** (100 MHz, DMSO-d_6) δ 158.1, 156.6, 156.2, 154.7, 150.1, 148.7, 135.5, 132.2, 130.1, 126.6, 123.7, 118.7, 118.6, 107.2, 104.1, 99.8, 57.0, 56.4; **LC-MS** (ESI+) *m/z*: $[M+H]^+$Calcd for $C_{22}H_{20}N_3O_3$ 374.2; Found 374.3.

The freebase of **APS-1-68-2**: the hydrochloride salt was suspended in a mixture of water and 95:5 CH_2Cl_2/MeOH, and then the pH of the aqueous phase was adjusted to 7-8 with a saturated solution of $NaHCO_3$. The mixture was transferred to a separatory funnel, the layers were separated and the aqueous phase was extracted with a 95:5 mixture of CH_2Cl_2/MeOH (X2). The organic extracts were pooled, dried (Na_2SO_4), filtered and concentrated to dryness: **^{1}H NMR** (400 MHz, DMSO-d_6) δ 9.49 (br s, 1H), 8.44 (s, 1H), 7.84 (s, 1H), 7.78 (d, *J* = 9.0 Hz; 2H), 7.43-7.36 (m, 2H), 7.18 (s, 1H), 7.15-7.10 (m, 1H), 7.08 (d, *J* = 9.0 Hz; 1H), 7.05-7.00 (m, 2H), 3.96 (s, 3H), 3.93 (s, 3H).

6,7-Dimethoxy-N-(4-methoxyphenyl)quinazolin-4-amine hydrochloride (APS-1-70-1)—An 8 mL vial was charged with 4-chloro-6,7-dimethoxyquinazoline (56.2 mg, 0.250 mmol), 4-methoxyaniline (33.9 mg, 0.275 mmol) and 2-PrOH (2.5 mL). The mixture was stirred and heated at 70 °C for 14 h. After the reaction mixture had cooled to room temperature the solid was collected by vacuum filtration through a pipet filter (balled up piece of a Kimwipe in a 4 mL pipet) and then washed with 2-PrOH (X1) (X2). Air-drying yielded 40.0 mg (46%) of the title compound as a pale-yellow solid: **^{1}H NMR** (400 MHz, DMSO-d_6) δ 11.21 (br s, 1H), 8.73 (s, 1H), 8.26 (s, 1H), 7.58 (d, *J* = 9.2 Hz; 2H), 7.33 (s, 1H), 7.04 (d, *J* = 9.2 Hz; 2H), 4.00 (s, 3H), 3.98 (s, 3H), 3.80 (s, 3H); **^{13}C NMR** (100 MHz, DMSO-d_6) δ 158.0, 157.5, 156.0, 150.0, 149.0, 136.0, 129.7, 126.2, 113.9, 107.2, 103.8, 100.2, 56.8, 56.4, 55.4; **LC-MS** (ESI+) *m/z*: $[M+H]^+$Calcd for $C_{17}H_{18}N_3O_3$ 312.1; Found 312.3.

4-((6,7-Dimethoxyquinazolin-4-yl)amino)phenol hydrochloride (APS-1-82-1)—A 20 mL vial was charged with 4-chloro-6,7-dimethoxyquinazoline (225 mg, 1.00 mmol), 4-aminophenol (120 mg, 1.10 mmol) and 2-PrOH (5 mL). The mixture was stirred rapidly and heated at 70 °C for 7 h. After the reaction mixture had cooled to room temperature the solid was collected by vacuum filtration and washed with hexanes (X2). Air-drying yielded 293 mg (88%) of the title compound as a yellow solid: **^{1}H NMR** (400 MHz, DMSO-d_6) δ 14.83 (br s, 1H), 11.28 (br s, 1H), 9.70 (br s, 1H), 8.73 (s, 1H), 8.28 (s, 1H), 7.43 (d, *J* = 9.0 Hz; 2H), 7.35 (s, 1H), 6.86 (d, *J* = 9.0 Hz; 2H), 3.99 (s, 3H), 3.97 (s, 3H); **^{13}C NMR** (100 MHz, DMSO-d_6) δ 158.0, 156.0, 150.0, 148.6, 135.1, 127.9, 126.4, 115.2, 107.0, 104.0, 99.72, 99.70, 56.9, 56.4; **LC-MS** (ESI+) *m/z*: $[M+H]^+$Calcd for $C_{16}H_{16}N_3O_3$ 298.1; Found 298.3.

N-(4-(Benzyloxy)phenyl)-6,7-dimethoxyquinazolin-4-amine 2,2,2-trifluoroacetate (APS-2-12)—An 8 mL vial was charged with **APS-1-82-1** (100 mg, 0.300 mmol), K_2CO_3 (92 mg, 0.67 mmol) and dry DMF (2 mL). To the stirred mixture was added benzyl bromide (44 μL, 0.37 mmol) dropwise (<1 min) via syringe. The reaction was blanketed with argon and the vial was sealed with a screw cap. The mixture was heated at 60 °C and stirred for 16h. The resulting solution was allowed to cool to room temperature, then water (6 mL) was added and stirring was continued for 5 min. The precipitate that formed was isolated by vacuum filtration and washed with water (1 mL). The collected yellow solid was purified by silica gel chromatography (25 g cartridge), eluting at 20 mL/min and using a linear gradient of CH_2Cl_2/MeOH: 100:0→80:20 over 20 column volumes. The appropriate fractions were pooled and concentrated under vacuum to yield 92 mg (79%) of the freebase of **APS-2-12** as a white solid. The TFA salt was synthesized for

direct comparison with a commercial sample: The freebase was stirred for 15 min in a mixture of MeOH and TFA (1.05 equiv) and then the solution was concentrated to dryness. The remaining residue was triturated with Et_2O, and the resulting precipitate was collected by vacuum filtration. The isolated solid was washed with Et_2O (X1) and hexanes (X1), and then air-dried. Further drying under high vacuum provided the title compound as a yellow solid: **^{1}H NMR** (400 MHz, DMSO-d_6) δ 10.90 (br s, 1H), 8.74 (s, 1H), 8.03 (s, 1H), 7.54 (d, *J* = 9.0 Hz; 2H), 7.50-7.45 (m, 2H), 7.44-7.38 (m, 2H), 7.38-7.32 (m, 1H), 7.30 (s, 1H), 7.13 (d, *J* = 9.0 Hz; 1H), 5.16 (s, 2H), 3.98 (s, 3H), 3.97 (s, 3H); **^{13}C NMR** (100 MHz, DMSO-d_6) δ 158.3, 158.00, 157.97, 157.69, 156.5, 156.0, 150.0, 149.3, 136.9, 136.3, 129.8, 128.5, 127.9, 127.7, 126.1, 118.5, 115.6, 114.9, 107.1, 103.2, 100.6, 69.4, 56.5, 56.4; **LC-MS** (ESI+) *m/z*: $[M+H]^+$Calcd for $C_{23}H_{22}N_3O_3$ 388.2; Found 388.3.

6,7-Dimethoxy-N-(4-phenoxyphenyl)quinolin-4-amine hydrochloride (APS-2-16)—An 8 mL vial was charged with 4-chloro-6,7-dimethoxyquinoline (50.0 mg, 0.224 mmol), 4-phenoxyaniline (45.6 mg, 0.246 mmol) and 2-propanol (1 mL). To the stirred mixture was added 1.0 M HCl (50 μL, 0.05 mmol, 22 mol%) via syringe. The vial was sealed with a screw cap and the mixture was heated at 70 °C for 16 h. The reaction was allowed to cool to room temperature and the precipitate was isolated by vacuum filtration; the collected solid was washed with hexanes (X1). Air-drying yielded 84.0 mg (92%) of the title compound as a light-yellow solid: **^{1}H NMR** (400 MHz, DMSO-d_6) δ 14.42 (br s, 1H), 10.79 (s, 1H), 8.32 (d, *J* = 6.8 Hz; 1H), 8.21 (s, 1H), 7.51-7.41 (m, 5H), 7.22-7.14 (m, 3H), 7.13-7.07 (m, 2H), 6.68 (d, *J* = 6.8 Hz; 1H), 4.00 (s, 3H), 3.96 (s, 3H); **^{13}C NMR** (100 MHz, DMSO-d_6) δ 156.3, 155.4, 154.5, 153.4, 149.4, 139.7, 135.2, 132.6, 130.2, 127.4, 123.8, 119.6, 118.9, 111.5, 102.8, 99.8, 99.0, 56.8, 56.1; **LC-MS** (ESI+) *m/z*: $[M+H]^+$Calcd for $C_{23}H_{21}N_2O_3$ 373.2; Found 373.3.

4-(6,7-Dimethoxyquinazoline-4-ylamino)-3-methylphenol hydrochloride (APS-2-77)—A 20 mL vial (with screwcap) was charged with 4-chloro-6,7-dimethoxyquinazoline (112 mg, 0.500 mmol), 4-amino-3-methylphenol (67.7 mg, 0.550 mmol) and 2-propanol (6 mL). The vial was sealed and the mixture was stirred and heated at 78 °C for 22 h. After the reaction mixture had cooled to room temperature, the precipitate was collected by vacuum filtration and the solid was washed with 2-PrOH (X1), EtOAc (X1) and hexanes (X3). Air-drying yielded 151 mg (87%) of the title compound as a light-brown solid: **^{1}H NMR** (400 MHz, DMSO-d_6) δ 11.22 (br s, 1H), 9.63 (br s, 1H), 8.67 (s, 1H), 8.29 (s, 1H), 7.38 (s, 1H), 7.09 (d, *J* = 8.4 Hz; 1H) 6.76 (d, *J* = 2.4 Hz; 1H), 6.70 (dd, *J* = 8.4, 2.4 Hz; 1H), 3.984 (s, 3H), 3.978 (s, 3H), 2.10 (s, 3H) ppm; **^{13}C NMR** (100 MHz, DMSO-d_6) δ 159.2, 156.8, 156.1, 150.1, 148.7, 136.1, 135.1, 128.5, 126.4, 117.0, 113.2, 106.7, 104.0, 99.7, 56.8, 56.4, 18.0 ppm; **LC-MS** (ESI+) m/z: $[M+H]^+$Calcd for $C_{17}H_{18}N_3O_3$ 312.1, Found 312.1.

6,7-Dimethoxy-N-(2-methyl-4-phenoxyphenyl)quinazolin-4-amine 2,2,2-trifluoroacetate (APS-2-79)—An oven-dried 8 mL vial (with sepcap), under nitrogen, was charged with copper(I) iodide (3.2 mg, 0.017 mmol, 10 mol%), picolinic acid (4.2 mg, 0.034 mmol, 20 mol%), K_3PO_4 (108 mg, 0.509 mmol) and dry DMSO (1 mL). After the mixture had stirred for 20 min, **APS-2-77** (59.2 mg, 0.170 mmol) and iodobenzene (20.0 μL,

0.179 mmol) were added. The deep-red mixture was heated at 90 °C and stirred for 20 h. The resulting brown mixture was allowed to cool to room temperature and then filtered through neutral alumina (pre-saturated in a 4 mL pipet) eluting with CH_2Cl_2/MeOH (95:5, *ca*. 20 mL). The filtrate was concentrated to leave a yellow-brown semi-solid, which was purified by reverse-phase chromatography, eluting at 20 mL/min and using a linear gradient of water (with 0.1% v/v TFA)/acetonitrile: 90:10→95:5 over 20 minutes. The appropriate fractions were pooled and concentrated to yield 46.0 mg (56%) of the title compound as a yellow solid: **^{1}H NMR** (400 MHz, DMSO-d_6) δ 11.01 (br s, 1H), 8.75 (s, 1H), 8.06 (s, 1H), 7.48-7.40 (m, 2H), 7.38-7.31 (m, 2H), 7.23-7.15 (m, 1H), 7.11-7.03 (m, 3H), 6.95 (dd, *J* = 8.6, 2.7 Hz; 1H) 4.00 (s, 3H), 3.98 (s, 3H), 2.18 (s, 3H) ppm; **^{13}C NMR** (100 MHz, DMSO-d_6) δ 159.2, 158.3, 157.9, 156.3, 156.0, 150.2, 149.2, 137.2, 135.6, 130.5, 130.2, 129.2, 123.8, 120.2, 118.9, 116.3, 106.7, 103.3, 100.1, 56.5, 17.8 ppm; **LC-MS** (ESI+) m/z: [M +H]$^+$Calcd for $C_{23}H_{22}N_3O_3$ 388.2, Found 388.3.

APS-2-79•HCl was synthesized via an alternative sequence: A 20 mL vial was charged with phenol (593 mg, 6.30 mmol), 4-fluoro-2-methyl-1-nitrobenzene (930 mg, 6.00 mmol), K_2CO_3 (875 mg, 6.33 mmol) and dry DMF (10 mL). The vial was sealed with a screw cap, heated at 80 °C and stirred for 10 h. After the reaction had cooled to room temperature, the mixture was partitioned between EtOAc (50 mL) and water (50 mL) in a separatory funnel. The layers were separated and the aqueous phase was extracted with EtOAc (2 × 50 mL). The organic extracts were pooled, washed with 1 M KOH (3 × 50 mL), half saturated brine (2 × 50 mL) and brine (50 mL), dried ($MgSO_4$) and filtered. The filtrate was concentrated under vacuum to leave 2-methyl-1-nitro-4-phenoxybenzene (**APS-5-1-1a**) as an orange oil, which was used without further purification: **LC-MS** (ESI+) m/z: [M+H]$^+$Calcd for $C_{13}H_{12}NO_3$ 230.1, Found 230.2.

To the flask (200 mL) containing **APS-5-1-1a** was added, Pd^0 (640 mg, 5% w/w on activated carbon, 0.30 mmol, 5 mol%) and then MeOH (60 mL). A stirrer bar was added to the flask and a three-way inlet-adapter (with a Teflon stopcock) was attached. The flask was evacuated (house vacuum) and backfilled with H_2 gas from a balloon (X5). The reaction mixture was stirred for 4h under positive H_2 pressure and then filtered through a pad (3 × 4 cm) of Celite under vacuum; the filter-cake was washed with MeOH (X2). The combined filtrates were concentrated under vacuum to yield 1.11 g (93%) of 2-methyl-4-phenoxyaniline (**APS-5-1-1**) as a dark oil, which was used in subsequent reactions without further purification: **LC-MS** (ESI+) *m/z*: [M+H]$^+$Calcd for $C_{13}H_{14}NO$ 200.1; Found 200.2.

A portion of the above prepared **APS-5-1-1** (112 mg, 0.562 mmol) was added to an 8 mL vial containing 4-chloro-6,7-dimethoxyquinazoline (105 mg, 0.467 mmol) and 2-PrOH (3 mL). The vial was sealed with a screw cap and the mixture was heated at 78 °C and stirred for 36 h. After the mixture had cooled to room temperature the precipitate was isolated by vacuum filtration (sintered glass funnel); the collected solid was washed with 2-PrOH (X2) and hexanes (X2). Air-drying yielded 170 mg (86%) of **APS-2-79•HCl** as a white solid: **^{1}H NMR** (400 MHz, DMSO-d_6) δ 14.93 (br s, 1H), 11.43 (br s, 1H), 8.73 (s, 1H), 8.35 (s, 1H), 7.47-7.40 (m, 2H), 7.38 (s, 1H), 7.33 (d, *J* = 8.6 Hz; 1H), 7.21-7.16 (m, 1H), 7.11-7.05 (m, 2H), 7.04 (d, *J* = 2.7 Hz; 1H), 6.93 (dd, *J* = 8.6, 2.7 Hz; 1H), 4.00 (s, 3H), 3.99 (s, 3H), 2.19 (s, 3H).

(Z)-N-(6,7-Dimethoxy-1-methylquinazolin-4(1H)-ylidene)-4-phenoxyaniline (APS-3-6)—An 8 mL vial was charged with K_2CO_3 (22.1 mg, 0.160 mmol), the freebase of **APS-1-68-2** (57.1 mg, 0.153 mmol) and dry DMF (0.5 mL). To the stirred mixture was added iodomethane (0.10 mL, 10% v/v solution in DMF, 0.16 mmol) dropwise (<1 min) via syringe. The headspace of the vial was purged with Ar and the vial was sealed with a screw cap. Two additional portions (0.02 mL) of iodomethane (total: 0.14 mL, 10% solution in DMF, 0.22 mmol) were added after 14 h and 20 h. The reaction mixture was stirred under Ar for another 16 h (36 h total) and then diluted with water (0.75 mL). The mixture was stirred rapidly for 15 min and the solid was collected by vacuum filtration (sintered glass funnel); the solid was washed with 1:1 isopropanol/water (X2) and then air-dried to provide 46.5 mg of a yellow solid. The solid was recrystallized from 1:1 MeOH/water (2 mL) to yield 26.5 mg (45%) of the title compound as a yellow solid: **^{1}H NMR** (400 MHz, DMSO-d_6) δ 7.90 (s, 1H), 7.67 (s, 1H), 7.39-7.32 (m, 2H), 7.10-7.02 (m, 3H), 6.99-6.94 (m, 2H), 6.93-6.87 (m, 3H), 3.93 (s, 3H), 3.85 (s, 3H), 3.61 (s, 3H); **^{13}C NMR** (100 MHz, DMSO-d_6) δ 158.0, 152.6, 152.0, 150.3, 149.8, 147.5, 147.1, 133.6, 129.8, 124.2, 122.4, 119.2, 117.5, 112.9, 106.4, 98.1, 56.0, 55.6, 36.4; **LC-MS** (ESI+) *m/z*: $[M+H]^+$Calcd for $C_{23}H_{22}N_3O_3$ 388.2; Found 388.3; the site of methylation was determined by NOESY analysis.

2,3-Dimethyl-1-nitro-4-phenoxybenzene (APS-3-72)—A 125 mL Erlenmeyer flask (containing a long, narrow stir bar) was charged with 2,3-dimethyl-4-nitrophenol (300 mg, 1.79 mmol), phenylboronic acid (328 mg, 2.60 mmol), copper(II) acetate (488 mg, 2.69 mmol), 4 Å molecular sieves (2 g, stored in an oven at 130 °C and finely-powdered with a mortar and pestle immediately prior to use) and CH_2Cl_2 (20 mL). Triethylamine (1.25 mL, 8.97 mmol) and pyridine (725 μL, 8.96 mmol) were added in a steady stream via syringe to the rapidly stirred reaction mixture. The mixture was stirred open to air for 48 h and then vacuum filtered through a pad (4 × 2 cm) of Celite, and the filter-cake was washed with CH_2Cl_2 (X2). The combined filtrates were concentrated under vacuum. The red-brown oil (377 mg) that remained was purified by silica gel chromatography (25 g cartridge), eluting at 20 mL/min and using a linear gradient of hexanes/EtOAc: 100:0→60:40 over 35 column volumes. The appropriate fractions were pooled and concentrated under vacuum to yield 127 mg (29%) of the title compound as a pink oil: **LC-MS** (ESI+) *m/z*: $[M+H]^+$Calcd for $C_{14}H_{14}NO_3$ 244.1; Found 244.1.

2,3-Dimethyl-4-phenoxyaniline (APS-3-76)—A 50 mL flask was charged with **APS-3-72** (127 mg, 0.522 mmol), Pd^0 (55.0 mg, 5% w/w on activated carbon, 0.026 mmol, 5 mol%) and MeOH (7 mL). A three-way inlet-adapter (with a Teflon stopcock) was attached to the flask, and the flask was evacuated and then backfilled with H_2 gas from a balloon (X5). The reaction mixture was stirred for 4h under positive H_2 pressure and then filtered through a plug of Celite (2 cm) in a pipet (4 mL) under positive N_2 gas pressure; the filter-cake was washed with MeOH (X2). The combined filtrates were concentrated to yield 109 mg (98%) of the title compound as a white solid: **LC-MS** (ESI+) *m/z*: $[M+H]^+$Calcd for $C_{14}H_{16}NO$ 214.1; Found 214.1.

N-(2,3-Dimethyl-4-phenoxyphenyl)-6,7-dimethoxyquinazolin-4-amine hydrochloride (APS-3-77)—An 8 mL vial was charged with **APS-3-76** (109 mg, 0.511

mmol), 4-chloro-6,7-dimethoxyquinazoline (95.7 mg, 0.426 mmol) and 2-PrOH (5 mL). The vial was sealed with a screw cap and the mixture was heated at 78 °C and stirred for 18 h. After the mixture had cooled to room temperature the solid was collected by vacuum filtration (sintered glass funnel); the solid was washed with 2-PrOH, EtOAc and hexanes. Air-drying yielded 168 mg (90%) of the title compound as a white solid: **^{1}H NMR** (400 MHz, DMSO-d_6) δ 14.83 (br s, 1H), 11.41 (br s, 1H), 8.72 (s, 1H), 8.32 (s, 1H), 7.42-7.35 (m, 3H), 7.21 (d, *J* = 8.7 Hz; 1H), 7.13-7.08 (m, 1H), 6.96-6.91 (m, 2H), 6.88 (d, *J* = 8.7 Hz; 1H), 4.01 (s, 3H), 4.00 (s, 3H), 2.19 (s, 3H), 2.15 (s, 3H); **^{13}C NMR** (100 MHz, DMSO-d_6) δ 159.2, 157.4, 156.2, 152.9, 150.2, 148.91, 148.89, 136.0, 131.4, 130.0, 129.1, 126.2, 122.7, 117.4, 117.1, 106.8, 104.0, 99.8, 56.8, 56.5, 15.0, 12.7; **LC-MS** (ESI+) *m/z*: [M +H]$^{+}$Calcd for $C_{24}H_{24}N_3O_3$ 402.2; Found 402.2.

Extended Data

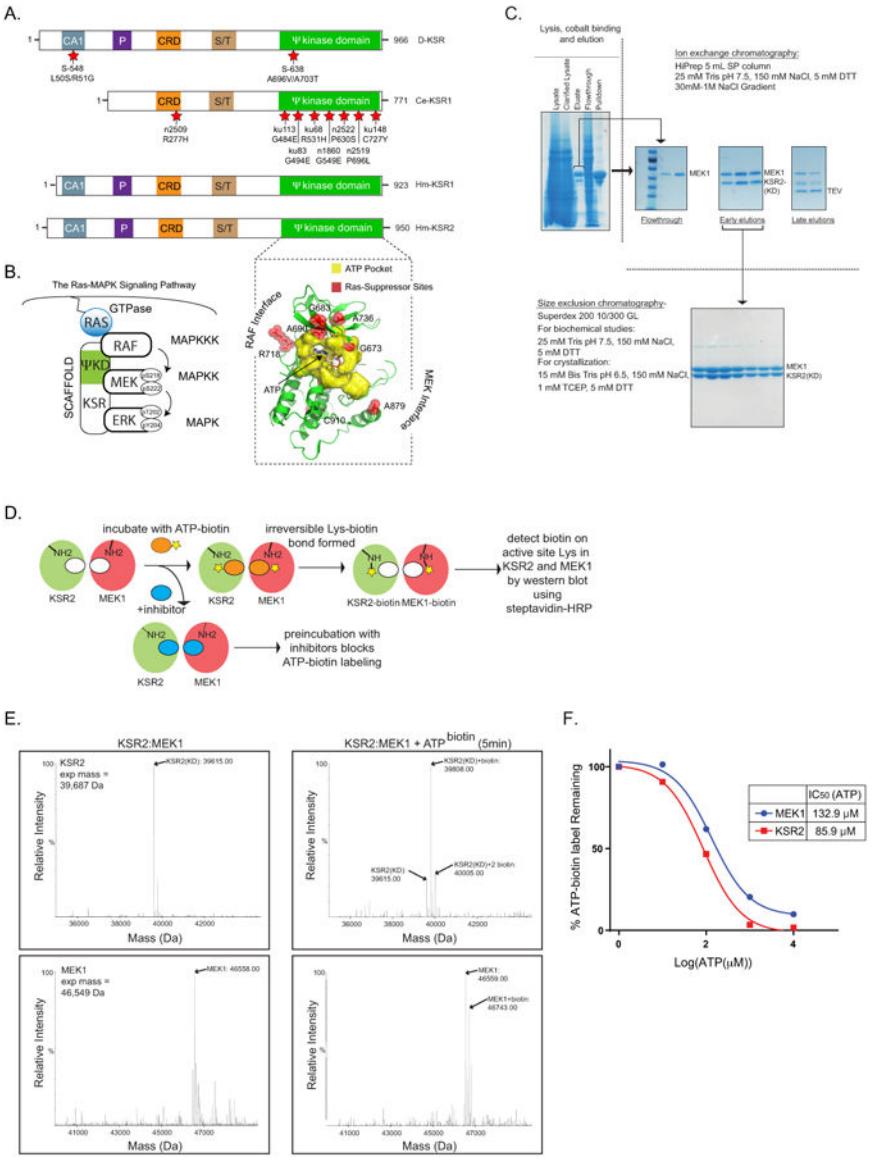

Extended Data Figure 1. Projection of Ras(G12V) suppressor alleles onto the primary and tertiary structure of KSR

a, Schematic representation of KSR from *Drosophila*, *Caenorhabditis elegans*, and KSR1 or KSR2 from humans. Suppressor mutations within KSR identified from forward genetic screens are highlighted with red stars. Allele names and corresponding mutations are given[3–5,15]. Two alleles in KSR found in the *Drosophila* screen are shown; one encoding for substitutions in a coil–coil SAM domain (CC-SAM) at the N terminus of *Drosophila* KSR (S548) and a second mutant in the predicted ATP-binding pocket of the KSR pseudokinase domain (S638). Eight distinct alleles were described in two separate studies conducted in *C. elegans*. The vast majority of the mutants localize to the pseudokinase domain of KSR and in particular ATP-contact residues (yellow). Residues highlighted in red and shown in the lower panel correspond to the human KSR2 residue equivalents of suppressor mutations

found in *Drosophila* and *C. elegans* orthologues. **b**, KSR is a scaffold for the Ras–MAPK signalling pathway. Phosphorylation of MEK1/2 at Ser218 and Ser222 by RAF, or ERK1/2 via phosphorylation at Thr202 and Tyr204 by MEK, are key events in signalling through the Ras–MAPK signalling pathway. **c**, Purification of the KSR2–MEK1 complex from insect cells. The KSR2 pseudokinase domain (KSR2(KD)) and MEK1 were co-expressed using the SF21 insect cell system. Lysis was performed by one freeze–thaw and sonication. Lysates were incubated with cobalt resin for 2 h and KSR2(KD)–MEK1 was eluted using a high-imidazole buffer. Eluate was then incubated with tomato etch virus (TEV) protease and λ -phosphatase overnight. The mixture was then applied to an ion-exchange column (Sp-HP) to separate stoichiometric KSR2–MEK1 complexes from free MEK1 and TEV. Fractions containing KSR2–MEK1 were applied to a gel-filtration column for final purification. **d**, Schematic of the ATP^{biotin} probe-labelling assay on KSR2–MEK1 complexes and screen for inhibitors. **e**, ATP^{biotin} directly labels KSR2 and MEK1 within purified complexes. Deconvoluted mass spectrum for KSR2–MEK1 complexes incubated with ATP^{biotin}. KSR2 and MEK1 spectra are included in the top and bottom panels, respectively. **f**, Graphical representation for ATP^{biotin} probe-labelling of KSR2–MEK1 complexes in the presence of increasing free ATP as shown in Fig. 1b. Corresponding IC_{50} values listed for both KSR2 and MEK1.

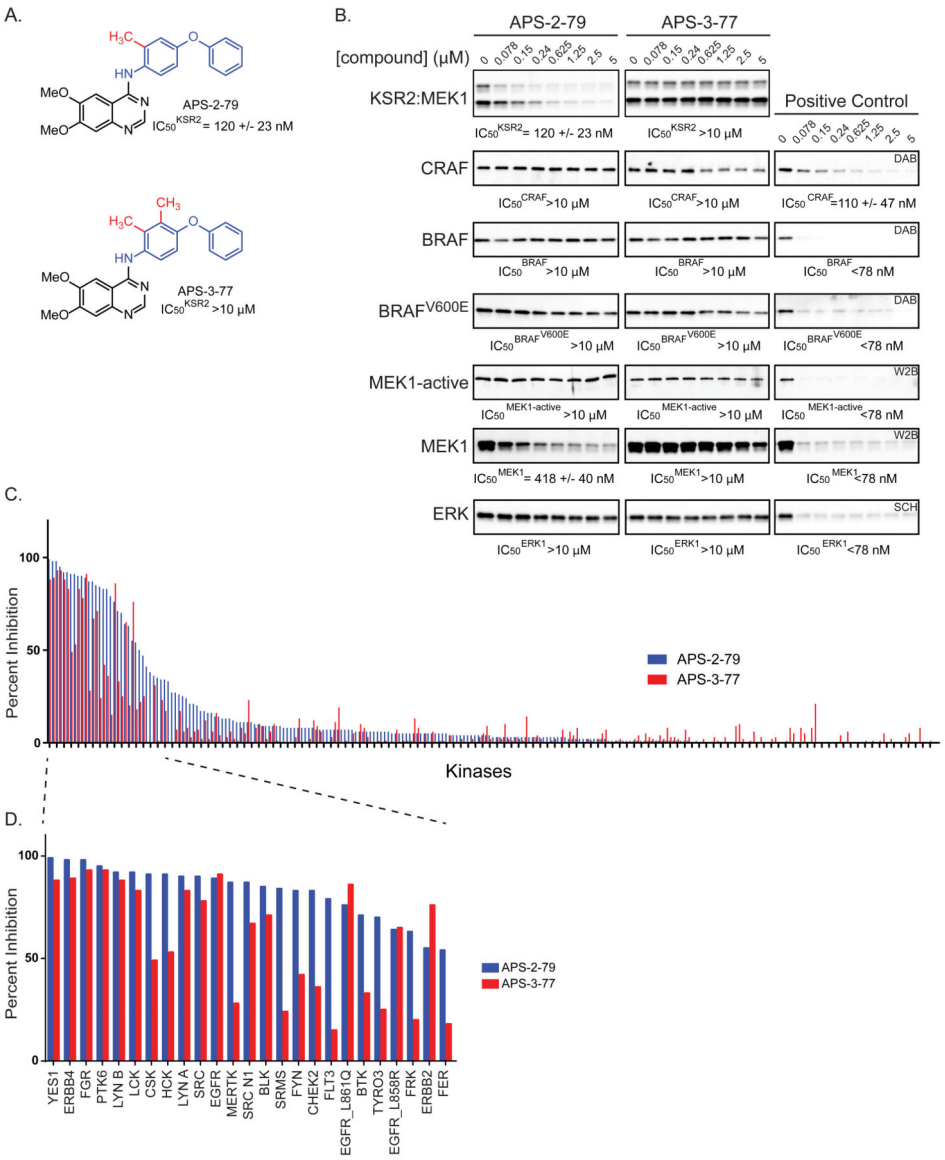

Extended Data Figure 2. APS-2-79 and APS-3-77 are positive and negative binders of KSR2

a, Chemical structures of APS-2-79 and APS-3-77 with respective IC_{50} values (mean ± s.d.; *n* = 2 biological replicates) for KSR2. **b**, Representative western blot images of *in vitro* ATP^{biotin} competition assays using recombinant MAPK family member proteins. Probe-labelling of the indicated kinases were measured in the presence of increasing concentrations of APS-2-79, APS-3-77, or a positive control compound. For CRAF, BRAF, and BRAF(V600E), the positive control was dabrafenib; for MEK1, the ATP-competitive inhibitor termed Wyeth-2b (ref. 28); and for ERK, SCH722984 (ref. 29). The listed IC_{50} values include mean ± s.d. based on two biological replicates. **c**, APS-3-77 and APS-2-79 share partially overlapping kinome-wide inhibitory profiles. The graph shows the percentage of inhibition of APS-2-79 and APS-3-77 (both at 1 μM) against 246 kinases. The raw data for this graph is in Supplementary Table 1. **d**, Inset showing the 25 kinases most inhibited by APS-2-79 and APS-3-77. Kinases with near-equal sensitivity to these inhibitors as measured

here include YES1, ERBB4, and FGR; variable sensitivity kinases include CSK, HCK, and MERTK.

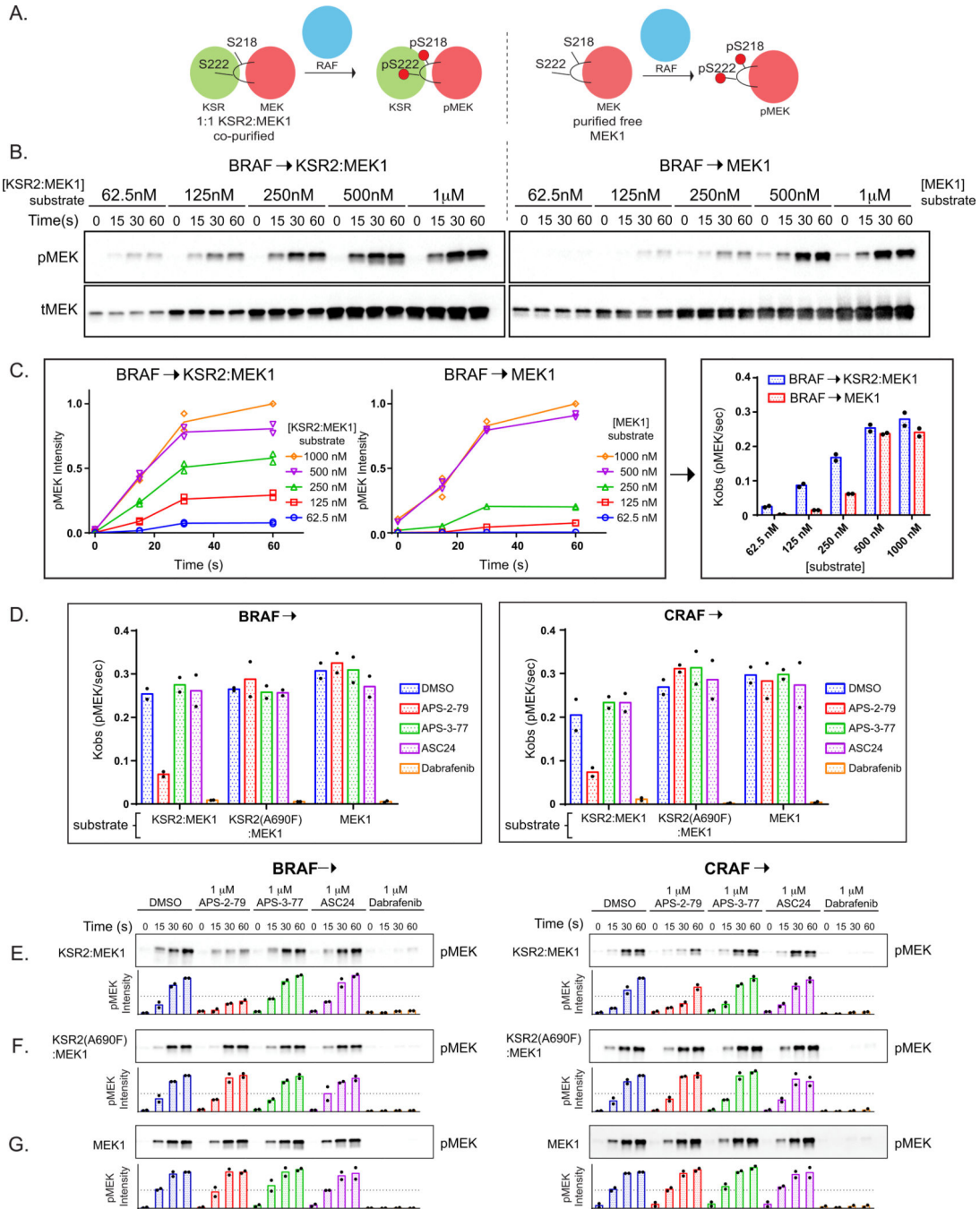

Extended Data Figure 3. APS-2-79 hinders RAF-mediated MEK phosphorylation in a KSR-dependent manner

a, Schematic of the RAF phosphorylation assay of free KSR2–MEK1 and MEK1. **b**, Phosphorylation of the indicated concentrations of MEK1 and the KSR2–MEK1 complex by BRAF (200 nM) in the presence of 1 mM ATP. Representative blots for phospho-MEK (top; as detected using a MEK1/2(pS218/pS222) antibody) and total MEK (tMEK; bottom) are

shown. **c**, Plots of pMEK versus time (seconds) at various concentrations of MEK1 and the KSR2–MEK1 complex. Bands were quantified and the phospho-MEK signal normalized relative to lane 20 in both panels. Data points of two biological replicates are included along each line. The rate of MEK phosphorylation (Kobs; pMEK per second; far right) are represented in bar graphs and are derived from the linear phase of the plots in the left hand panels. Bars represent mean of two biological replicates; values for each replicate are shown as points. **d**, Rates of BRAF (left) and CRAF (right) phosphorylation of the indicated MEK complexes (KSR2–MEK1; KSR2(A690F)–MEK1; and free MEK). Bars represent mean of two biological replicates; values for each replicate are shown as points. **e**–**g**, APS-2-79 inhibits BRAF and CRAF phosphorylation of MEK in a KSR-dependent manner. Phosphorylation of 500-nM KSR2–MEK1 (**e**), or KSR2(A690F)–MEK1 (**f**), and MEK1 (**g**) by BRAF (200 nM) or CRAF (10 nM) in the presence of 1-mM ATP and the indicated inhibitors. Representative western blots of phospho-MEK (as detected using a MEK1/2pS218/pS222 antibody) are shown. Bars represent mean of two biological replicates; individual data points of each replicate are shown.

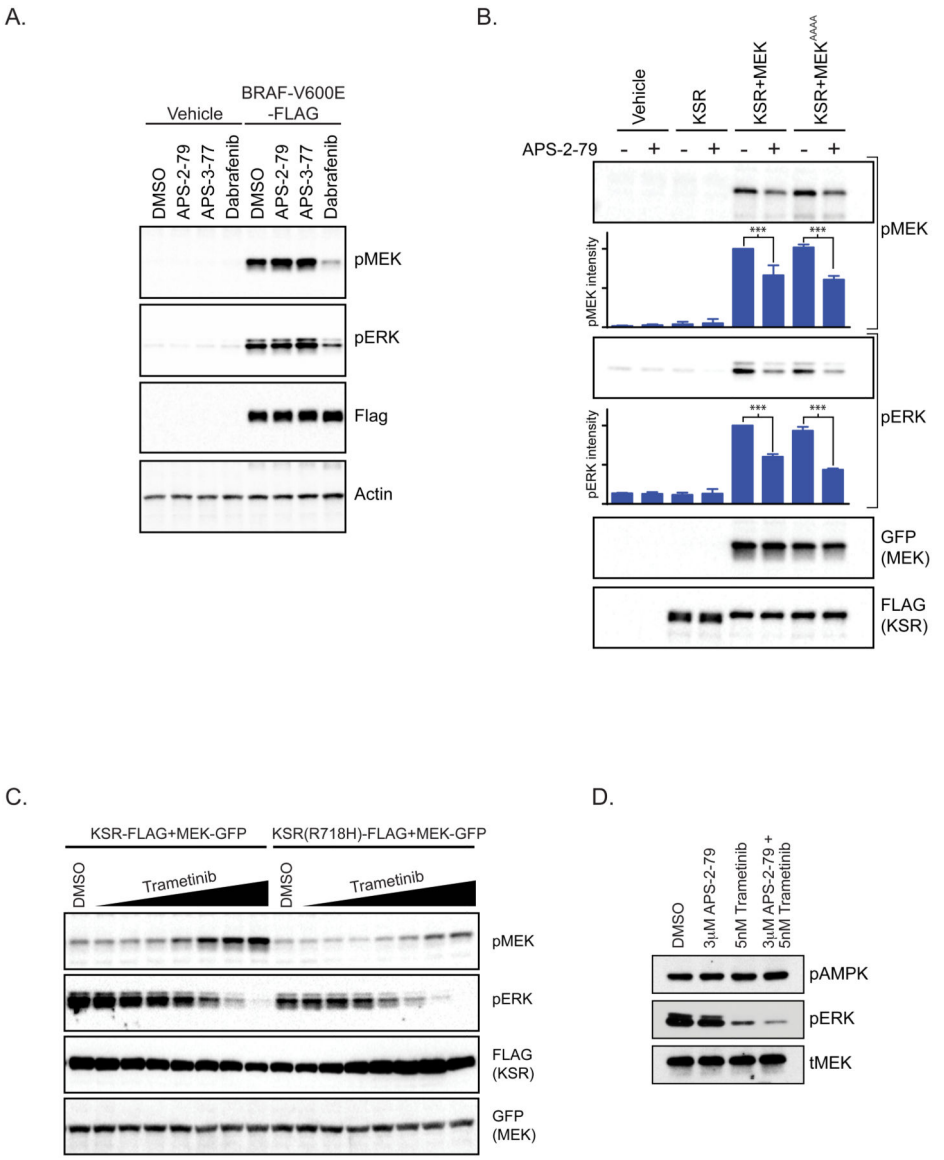

Extended Data Figure 4. APS-2-79 activity is not dependent on KSR phosphorylation sites in MEK or direct RAF inhibition

a, APS-2-79 does not affect BRAF(V600E)-induced MAPK activation in cells. BRAF(V600E)–Flag was expressed for 24 h in 293H cells. Cells were then treated for 2 h with DMSO or 5μM of either APS-2-79, APS-3-77, or dabrafenib before collection and western blot analysis of phosphorylated MEK (MEK1/2(pSer218/pSer222)) and ERK (ERK1/2(pT202/pY204)). **b**, Removal of putative KSR phosphorylation sites in MEK (MEK(AAAA); S18A, T23A, S24A, S72A; ref. 7) neither hinders KSR-dependent MAPK signalling, nor the activity of APS-2-79. Co-expression of full-length KSR–Flag and wild-type MEK1–GFP or MEK(AAAA)–GFP leads to enhanced MAPK signalling within 293H cells as visualized by immunoblotting for phosphorylated MEK (MEK1/2(pSer218/pSer222)) and ERK (ERK1/2(pT202/pY204)). APS-2-79 impedes KSR-stimulated MAPK signalling within cells through wild-type and MEK(AAAA) equally. Bars and error bars indicate pMEK and pERK intensity and standard deviations, respectively. Signals were

normalized relative to lane 5. Error bars indicate the mean ± s.d. (n = 3 biological replicates). ***P < 0.0005 by two-tailed unpaired t-testing. **c**, The dimer-deficient KSR(R718H) mutant, relative to wild-type KSR, is compromised in MEK-inhibitor-induced feedback. 293H cells were co-transfected with MEK–GFP and KSR–Flag or KSR(R718H)–Flag for 24 h and then treated with increasing concentrations of trametinib (range of 0.13 to 100 nM; threefold dilutions) for an additional 48 h. Cells were collected and analysed by western blot. **d**, Phospho-AMPK remains unchanged in HCT116 cells upon co-treatment with APS-2-79 and trametinib. HCT116 cells were treated with APS-2-79 and/or trametinib for 48 h. Phospho-AMPK (top), phospho-ERK(pERK), and total MEK (bottom) western blots are shown.

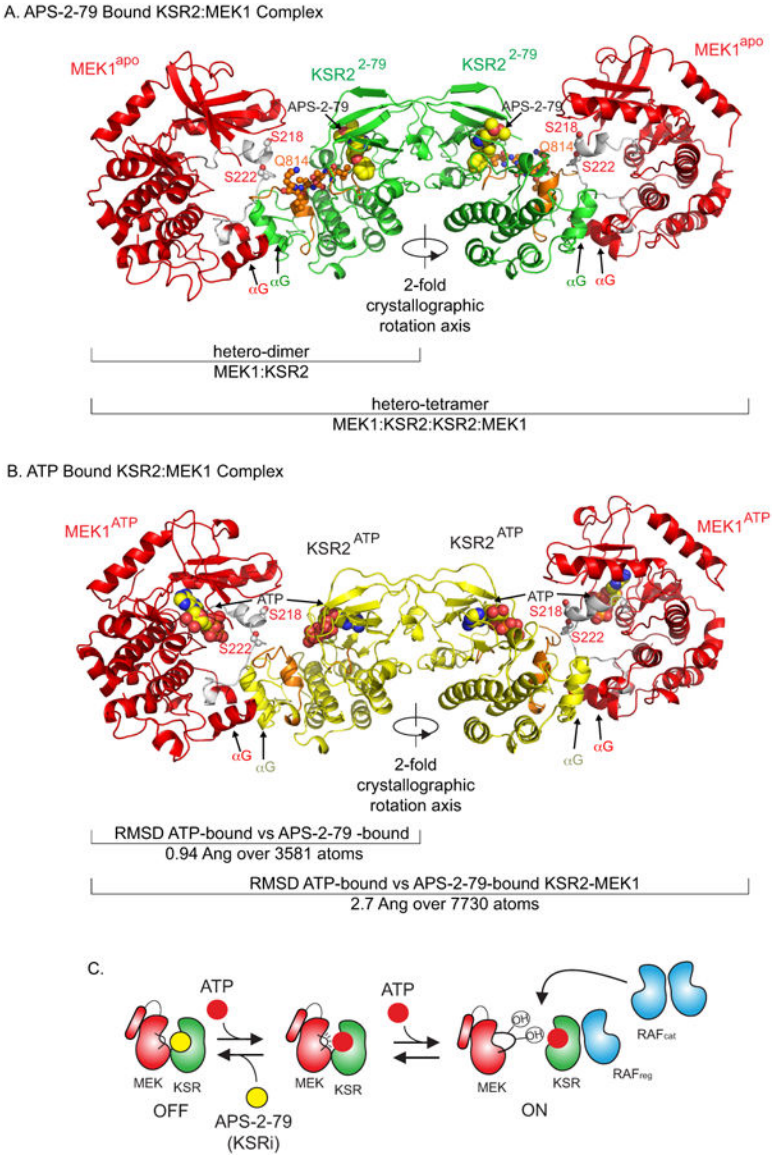

Extended Data Figure 5. Higher order assembly of the KSR2–MEK1 complex bound to ATP or APS-2-79

a, Assembly of the KSR2–MEK1 heterodimer bound to APS-2-79. A crystal-packing two-fold symmetry axis of the asymmetric unit containing a single KSR2–MEK1 complex produces the heterotetramer. KSR2 bound to APS-2-79 is coloured green, and MEK1 is coloured red. The activation segments of KSR2 and MEK1 are coloured orange and white, respectively. The ‘induced lock’ (residues 809 to 814) within KSR2 is highlighted as orange, red and blue spheres. **b**, Assembly of the KSR2–MEK1 heterodimer bound to ATP as reported ref. 7 (PDB code: 2Y4I). A crystallographic two-fold rotation axis produces the heterotetramer. r.m.s. deviation between the heterodimer and heterotetramers, respectively, of the ATP- and APS-2-79-bound KSR2–MEK1 complexes are listed below. **c**, A model for APS-2-79 function as a KSR-targeted antagonist of MAPK signalling. APS-2-79 shifts the equilibrium of KSR2–MEK1 complexes so to populate the OFF state (left), and thereby antagonizes RAF dimerization and subsequent phosphorylation of KSR-bound MEK (far right). The model for RAF dimerization and MEK phosphorylation are adapted from ref. 7. In this model, the role of RAF_{cat} may be fulfilled by multiple active RAF-family kinases, such as C-RAF, bound within homo- or heterodimers of RAF–RAF or KSR–RAF, respectively.

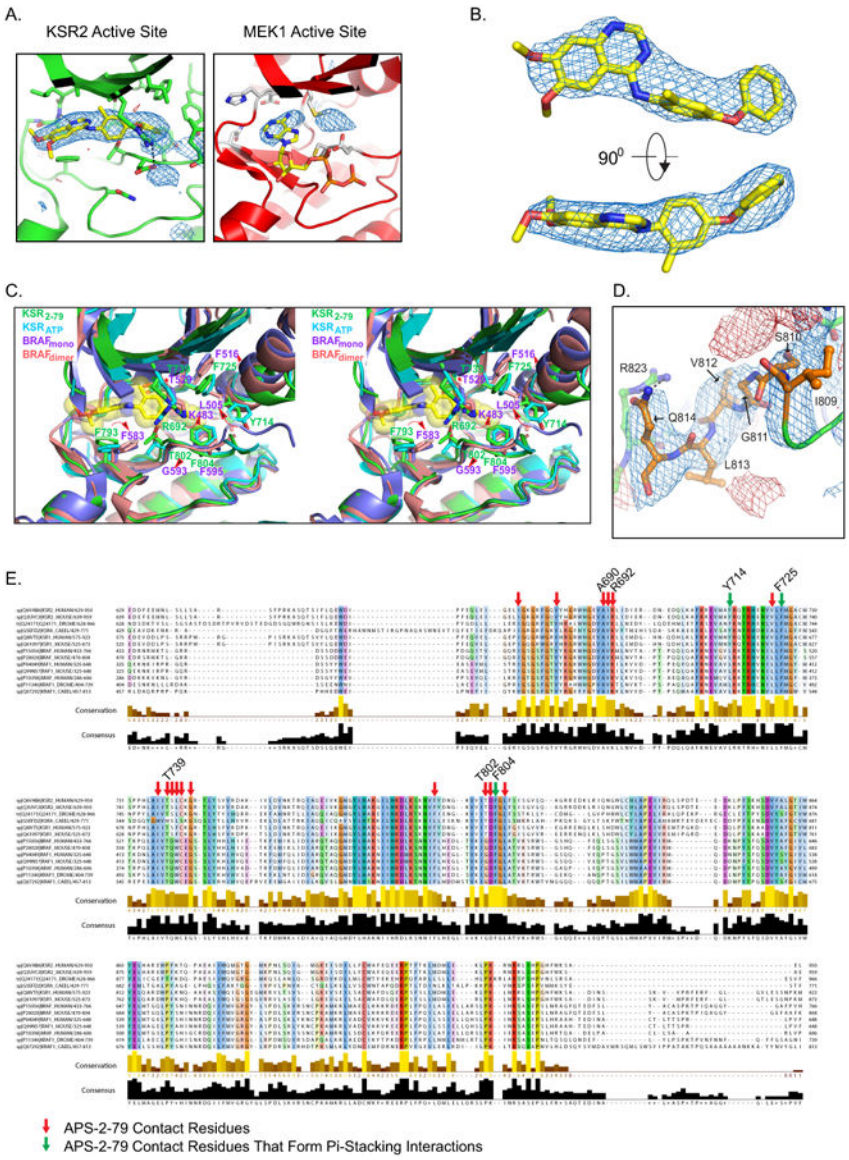

Extended Data Figure 6. The APS-2-79 binding site within KSR2 and possible basis for KSR over RAF selectivity

a, APS-2-79 and ATP are overlaid in the KSR2 and MEK1 active sites, respectively. ATP was shown here to emphasize the MEK active site, but ATP was not included in the final model. Positive (blue) and negative (red) $F_o - F_c$ electron density maps, calculated before modelling of APS-2-79, are contoured at 3.5σ. Strong-positive-difference density within KSR2 supported modelling of APS-2-79 bound to KSR2 within the KSR2–MEK1 complex. **b**, Electron density map (blue mesh) for APS-2-79 (sticks) contoured at 4.5σ. Map represents positive difference density within the KSR2 active site before modelling of APS-2-79. **c**, Superposition of KSR2 (ATP- and APS-2-79-bound) with BRAF monomer (PDB code: 4W05) and BRAF dimer (PDB code: 3C4C) co-crystal structures reveals the possible bases for selectivity of APS-2-79 for KSR over RAF proteins. Residues within the APS-2-79 binding pocket that diverge between KSR and RAF proteins, but which are highly conserved within both sub-families are indicated with arrows. Thr802 in KSR2, which is

universally a Gly residue in all active RAF homologues, and also Phe516 and Phe793 in KSR2, which adopt distinct orientations from the equivalent Phe residues in RAF kinases, directly contact the biphenyl ether motif in APS-2-79. The T802G substitution, as well as the positional differences of the above-mentioned aromatic residues, would be predicted to reduce binding of active RAFs with APS-2-79. Another interaction that is probably favoured in KSR includes the contact mediated by the epsilon nitrogen of Arg692 with the –O- linker of the biphenyl motif; the placement of Arg692 is stabilized by Asp803 of the DFG motif. In RAF, the Arg-to-Lys substitution (Lys483 in subdomain II of BRAF), lacks the equivalent nitrogens to bond with both the –O- linker in APS-2-79 and the aspartate of the DFG motif. **d**, Positive (blue) and negative (red) $F_o - F_c$ electron density map contoured at $\pm 2.5\sigma$, before modelling of residues I809 to Q814 in KSR2, is shown. **e**, Sequence alignment of KSR and RAF proteins. Arrows highlight APS-2-79 contact residues.

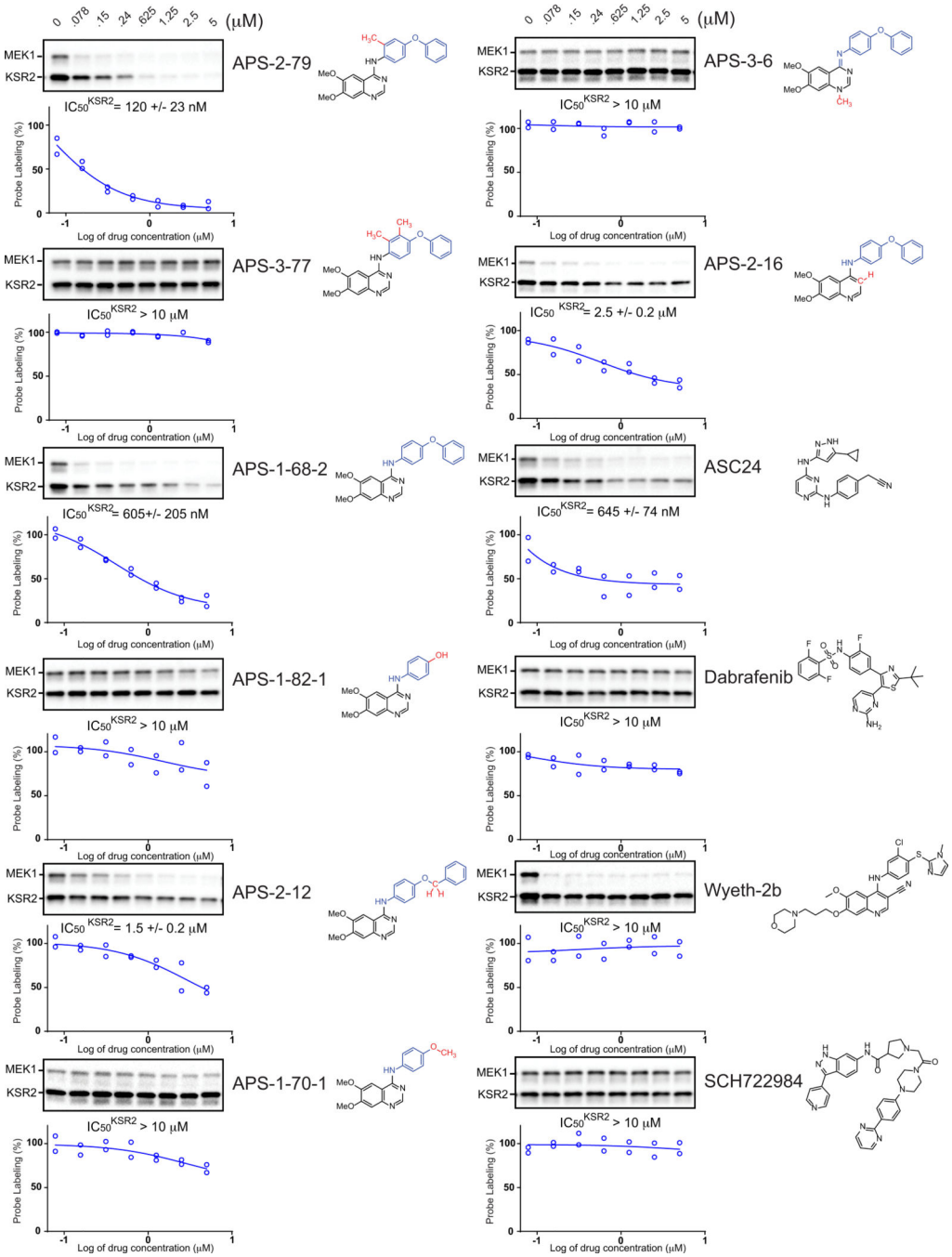

Extended Data Figure 7. *In vitro* AT P^{biotin} competition assays

Representative western blot images of *in vitro* ATP^{biotin} competition assays using recombinant KSR2–MEK1 and analogues reported in this study. Chemical structures are shown adjacent to assay blots. IC_{50} values (mean ±s.d.; n = 2 biological replicates) against ATP^{biotin} probe-labelling of KSR2 are listed below blots. Line graphs include data points from two biological replicates.

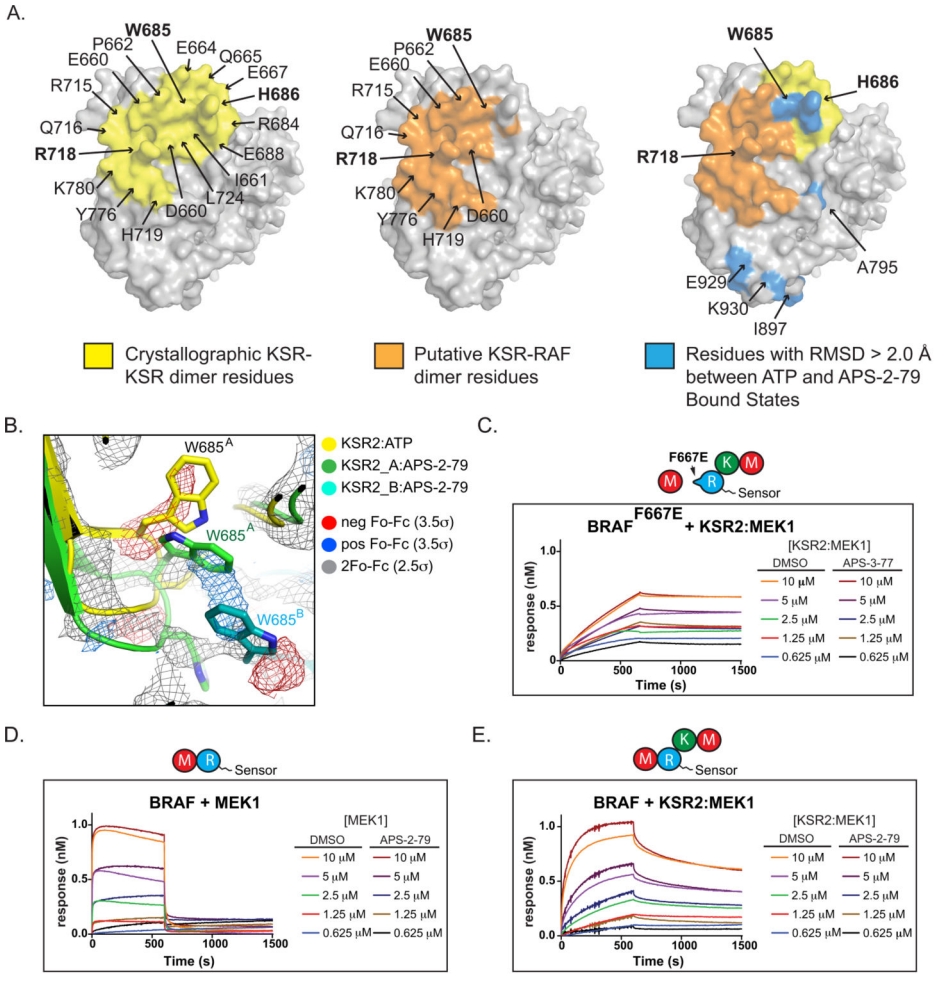

F.

	Figure Panel	Sensor	Protein	Treatment	Binding Model	Kd (M)	Kon(1/Ms)	Koff(1/s)	Fit X^2	Fit R^2
1	Fig. 3D	BRAF^{F667E}	KSR2:MEK1	DMSO	1:1'	1.99E-06	5.30E+02	1.06E-03	0.4664	0.9921
2	Ext. Fig. 8C	BRAF^{F667E}	KSR2:MEK1	APS-3-77	1:1'	2.55E-06	3.35E+02	8.56E-04	1.3578	0.9952
3	Fig. 3G	BRAF^{F667E}	KSR2:MEK1	APS-2-79	No binding	-	-	-	-	-
4	Fig. 3E	BRAF^{F667E}	MEK1	DMSO	No binding	-	-	-	-	-
5	Fig. 3C	BRAF	MEK1	DMSO	1:1'	5.17E-08	2.09E+05	1.49E+04	1.958	0.9875
6	Ext. Fig. 8D	BRAF	MEK1	APS-2-79	1:1'	4.04E-08	1.65E+05	1.64E+04	2.252	0.9546
7	Fig. 3A	BRAF	KSR2:MEK1	DMSO	non-1:1	-	-	-	-	-
8	Ext. Fig. 8E	BRAF	KSR2:MEK1	APS-2-79	non-1:1	-	-	-	-	-
9	Fig. 3F	BRAF$^{F667E/R509H}$	KSR2:MEK1	DMSO	No binding	-	-	-	-	-

Extended Data Figure 8. Bio-layer inferometry binding data between BRAF and free MEK1 or the KSR2–MEK1 complex

a, Mapping of residues with a r.m.s. deviation of greater than 2.0 Angstrom between the ATP- and APS-2-79-bound states of KSR2–MEK1 (right, blue), highlights alterations at contact residues Trp685 and His686 within the KSR–KSR homodimer (left, yellow) and KSR–RAF heterodimer (middle, orange) interfaces. **b**, Movement of Trp685–His686 within KSR2 between the ATP- and APS-2-79-bound states. A single protomer of KSR2 in the ATP-bound state (yellow), and both protomers (green and cyan) of the KSR2 dimer within

the APS-2-79-bound state, are shown. Negative density around W685 and His686 in early-stage maps supported the conformational change in this loop between the ATP- and APS-2-79-bound states. **c**, The negative control compound APS-3-77 (25 μM) does not impact assembly of BRAF(F667E) and KSR2–MEK1. These assays were performed identically to the experiments in Fig. 3b–g. Coloured curves indicate dose ranges of KSR2–MEK1 or MEK1 from 625 nM to 10 μM in the presence or absence of the indicated compounds. In all plots, association occurred from 0 to 660 s, and dissociation was monitored thereafter up to 1500 s. **d**–**e**, Biolayer inferometry of wild-type BRAF with MEK1 and KSR2–MEK1 in the presence of DMSO and 25 μM APS-2-79. These assays were performed identically to the experiments in Fig. 3b–g. Coloured curves indicate dose ranges of KSR2–MEK1 or MEK1 from 625 nM to 10 μM in the presence or absence of the indicated compounds. In all plots, association occurred from 0 to 660 s, and dissociation was monitored thereafter up to 1500 s. **f**, Table summary of BLI data in this figure and Fig. 3b–h. K_d, K_{on}, and K_{off} values represent the mean and s.e.m. measurements derived from global fitting of 5 binding curves. χ^2 and R^2 describe experimental and model data correlations; < 3 and above 0.95, respectively, indicate good fits.

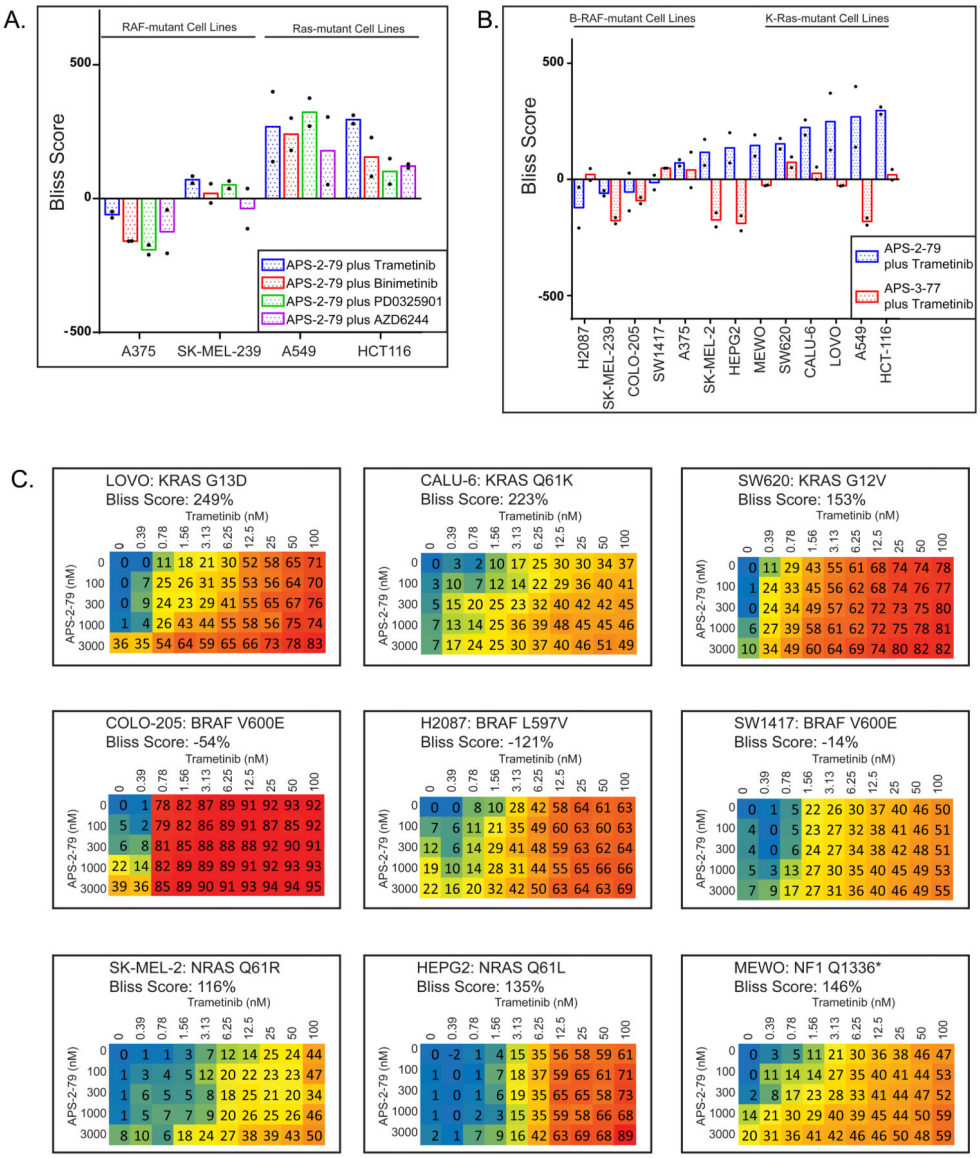

Extended Data Figure 9. KSRi binder APS-2-79 synergizes with trametinib in Ras-mutant cells

a, Average Bliss score of the combination of trametinib, binimetinib, PD0325901, or AZD6244 with APS-2-79 in the Ras-mutant cell lines HCT116 and A549 versus the RAF-mutant cell lines A375 and SK-MEL-239. Full combination matrices of APS-2-79 (range: 100 nM to 3 μM in threefold dilutions) with trametinib (range: 0.01–100 nM in threefold dilutions), binimetinib (range: 0.1–10 μM in threefold dilutions), PD0325901 (range: 0.1–10 μM in threefold dilutions), and AZD6244 (range: 0.1–10 μM in threefold dilutions). Bars represent the mean Bliss scores calculated from two biological replicates of the depicted concentration matrices; points represent each calculated score. **b**, Average Bliss scores of APS-2-79 or APS-3-77 in combination with trametinib in RAF-mutant, RAS-mutant cell lines. SK-MEL-2 and HepG2 are N-Ras-mutant cell lines, and MEWO is a NF1-mutant cell line. Bars represent the mean Bliss scores calculated from two biological replicates of the depicted concentration matrices; points represent each calculated score. **c**, Complete cell

viability analysis of APS-2-79 (range: 100–3,000 nM in threefold dilutions) plus trametinib (range: 0.01–100 nM in threefold dilution) over a full concentration matrix in the Ras-mutant LOVO, CALU-6, SW620, SK-MEL-2, and HEPG2 cell lines, the RAF-mutant COLO-205, H2087, and SW1417 cells, and the NF1-mutant MEWO cell line. Numbers listed within synergy matrices represent percentage of growth inhibition relative to DMSO control and are the mean of two biological replicates. Bliss scores represent the mean calculated from two biological replicates of the depicted concentration matrices.

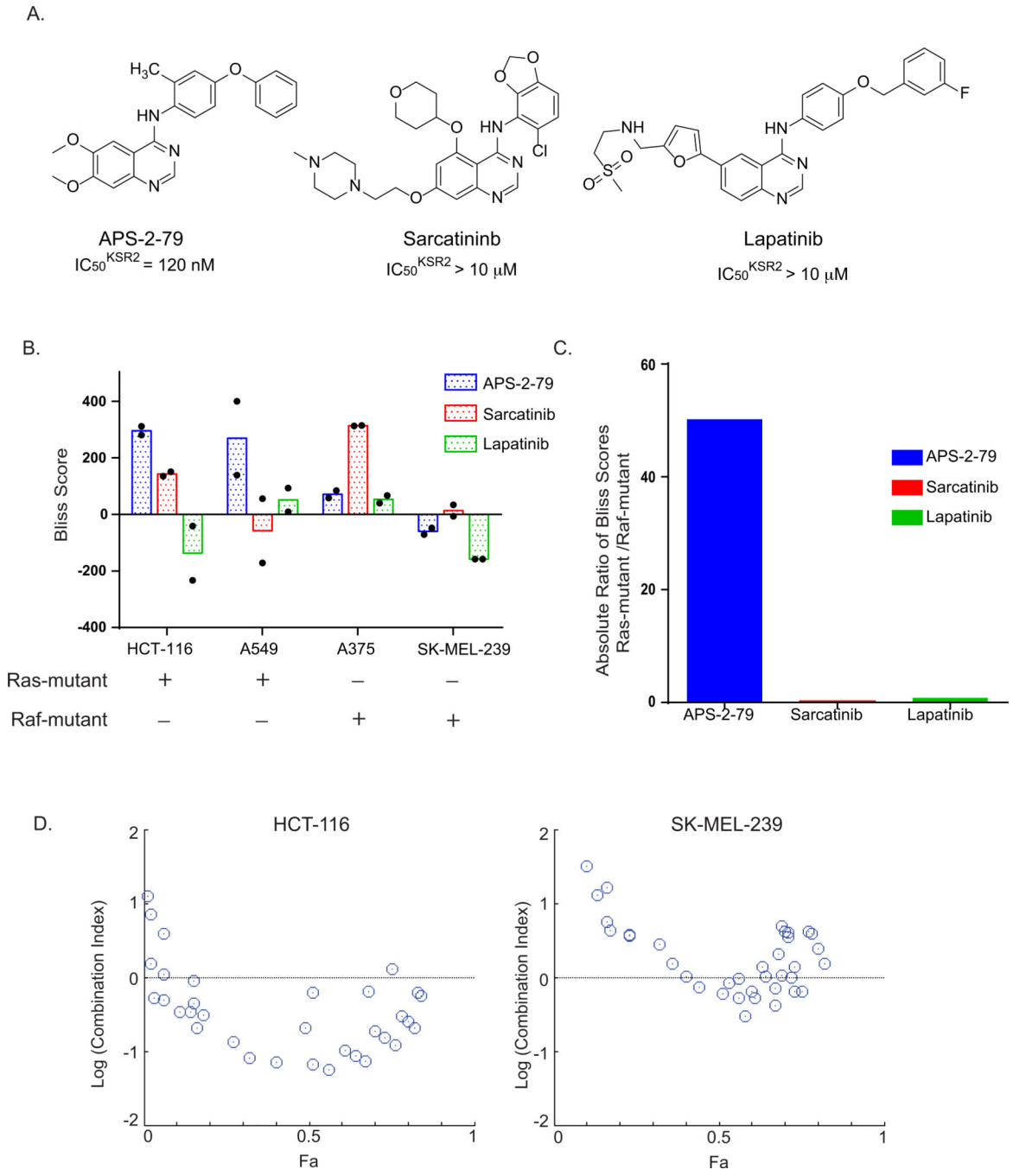

Extended Data Figure 10. APS-2-79 synergizes with trametinib specifically in Ras-mutant cells compared to the HER-family and SRC-family inhibitors lapatinib and sarcatinib

a, Chemical structures of APS-2-79 and quinazoline-containing kinase inhibitors sarcatinib and lapatinib. The primary targets for sarcatinib and lapatinib are c-Src and Her2, respectively[30]. IC_{50} values against ATP^{biotin} probe-labelling of KSR2 are listed below structures. b, Bliss score analysis of HCT-116, A549, A375 and SK-MEL-239 cells treated with APS-2-79, sarcatinib, or lapatinib (range: 100–3,000 in threefold dilutions) in combination with trametinib (range: 0.01–100 in threefold dilution). Bars represent the mean Bliss scores calculated from two biological replicates; points represent each calculated score. c, Absolute Bliss score of the indicated drugs in combination with trametinib in Ras-mutant relative to RAF-mutant cell lines demonstrates selective synergy in Ras-mutant cell lines for APS-2-79 compared to sarcatinib and lapatinib. d, log of the combination index graphs of APS-2-79 in combination with trametinib in HCT-116 versus SK-MEL-239 cells as compared to the fractional effect. Negative combination index over a broad fractional effect range within HCT-116, but not SK-MEL-239, indicates strong synergy.

Supplementary Material

Refer to Web version on PubMed Central for supplementary material.

Acknowledgments

We thank K. Shokat, R. Fisher, R. Cagan, S. Aaronson, M. Lazarus, E. Bernstein, and members of the Dar laboratory for comments on the manuscript; A. Maldonado and L. Silber for technical support; and staff at the Advanced Photon Source (Beamline 23-ID-B) for help with X-ray diffraction experiments. The Dar laboratory is supported by innovation awards from the NIH (1DP2CA186570-01) and Damon Runyon-Rachleff Foundation. A.C.D. is a Pew-Stewart Scholar in Cancer Research and Young Investigator of the Pershing-Square Sohn Cancer Research Alliance.

References

1. Stephen AG, Esposito D, Bagni RK, McCormick F. Dragging ras back in the ring. Cancer Cell. 2014; 25:272–281. [PubMed: 24651010]
2. Lavoie H, Therrien M. Regulation of RAF protein kinases in ERK signalling. Nat Rev Mol Cell Biol. 2015; 16:281–298. [PubMed: 25907612]
3. Kornfeld K, Hom DB, Horvitz HR. The ksr-1 gene encodes a novel protein kinase involved in Ras-mediated signaling in *C. elegans*. Cell. 1995; 83:903–913. [PubMed: 8521514]
4. Sundaram M, Han M. The *C. elegans* ksr-1 gene encodes a novel Raf-related kinase involved in Ras-mediated signal transduction. Cell. 1995; 83:889–901. [PubMed: 8521513]
5. Therrien M, et al. KSR, a novel protein kinase required for RAS signal transduction. Cell. 1995; 83:879–888. [PubMed: 8521512]
6. Rajakulendran T, Sahmi M, Lefrançois M, Sicheri F, Therrien M. A dimerization-dependent mechanism drives RAF catalytic activation. Nature. 2009; 461:542–545. [PubMed: 19727074]
7. Brennan DF, et al. A Raf-induced allosteric transition of KSR stimulates phosphorylation of MEK. Nature. 2011; 472:366–369. [PubMed: 21441910]
8. Fernandez MR, Henry MD, Lewis RE. Kinase suppressor of Ras 2 (KSR2) regulates tumor cell transformation via AMPK. Mol Cell Biol. 2012; 32:3718–3731. [PubMed: 22801368]
9. Le Borgne M, Filbert EL, Shaw AS. Kinase suppressor of Ras 1 is not required for the generation of regulatory and memory T cells. PLoS One. 2013; 8:e57137. [PubMed: 23431403]
10. Nguyen A, et al. Kinase suppressor of Ras (KSR) is a scaffold which facilitates mitogen-activated protein kinase activation *in vivo*. Mol Cell Biol. 2002; 22:3035–3045. [PubMed: 11940661]

11. Michaud NR, et al. KSR stimulates Raf-1 activity in a kinase-independent manner. Proc Natl Acad Sci USA. 1997; 94:12792–12796. [PubMed: 9371754]
12. Roy F, Laberge G, Douziech M, Ferland-McCollough D, Therrien M. KSR is a scaffold required for activation of the ERK/MAPK module. Genes Dev. 2002; 16:427–438. [PubMed: 11850406]
13. Stewart S, et al. Kinase suppressor of Ras forms a multiprotein signaling complex and modulates MEK localization. Mol Cell Biol. 1999; 19:5523–5534. [PubMed: 10409742]
14. Samatar AA, Poulikakos PI. Targeting RAS-ERK signalling in cancer: promises and challenges. Nat Rev Drug Discov. 2014; 13:928–942. [PubMed: 25435214]
15. Karim FD, et al. A screen for genes that function downstream of Ras1 during *Drosophila* eye development. Genetics. 1996; 143:315–329. [PubMed: 8722784]
16. Hu J, et al. Allosteric activation of functionally asymmetric RAF kinase dimers. Cell. 2013; 154:1036–1046. [PubMed: 23993095]
17. Lavoie H, et al. Inhibitors that stabilize a closed RAF kinase domain conformation induce dimerization. Nat Chem Biol. 2013; 9:428–436. [PubMed: 23685672]
18. Douziech M, Sahmi M, Laberge G, Therrien M. A KSR/CNK complex mediated by HYP, a novel SAM domain-containing protein, regulates RAS-dependent RAF activation in Drosophila. Genes Dev. 2006; 20:807–819. [PubMed: 16600912]
19. McKay MM, Ritt DA, Morrison DK. Signaling dynamics of the KSR1 scafold complex. Proc Natl Acad Sci USA. 2009; 106:11022–11027. [PubMed: 19541618]
20. Haling JR, et al. Structure of the BRAF-MEK complex reveals a kinase activity independent role for BRAF in MAPK signaling. Cancer Cell. 2014; 26:402–413. [PubMed: 25155755]
21. Chapman PB, Solit DB, Rosen N. Combination of RAF and MEK inhibition for the treatment of BRAF-mutated melanoma: feedback is not encouraged. Cancer Cell. 2014; 26:603–604. [PubMed: 25517746]
22. Hatzivassiliou G, et al. Mechanism of MEK inhibition determines efficacy in mutant KRAS- versus BRAF-driven cancers. Nature. 2013; 501:232–236. [PubMed: 23934108]
23. Lito P, et al. Disruption of CRAF-mediated MEK activation is required for effective MEK inhibition in KRAS mutant tumors. Cancer Cell. 2014; 25:697–710. [PubMed: 24746704]
24. Sos ML, et al. Oncogene mimicry as a mechanism of primary resistance to BRAF inhibitors. Cell Reports. 2014; 8:1037–1048. [PubMed: 25127139]
25. McKay MM, Ritt DA, Morrison DK. RAF inhibitor-induced KSR1/B-RAF binding and its effects on ERK cascade signaling. Curr Biol. 2011; 21:563–568. [PubMed: 21458265]
26. Xie T, et al. Pharmacological targeting of the pseudokinase Her3. Nat Chem Biol. 2014; 10:1006–1012. [PubMed: 25326665]
27. Zeqiraj E, Filippi BM, Deak M, Alessi DR, van Aalten DM. Structure of the LKB1-STRAD-MO25 complex reveals an allosteric mechanism of kinase activation. Science. 2009; 326:1707–1711. [PubMed: 19892943]
28. Mallon R, et al. Identification of 4-anilino-3-quinolinecarbonitrile inhibitors of mitogen-activated protein/extracellular signal-regulated kinase 1 kinase. Mol Cancer Ther. 2004; 3:755–762. [PubMed: 15210862]
29. Morris EJ, et al. Discovery of a novel ERK inhibitor with activity in models of acquired resistance to BRAF and MEK inhibitors. Cancer Discovery. 2013; 3:742–750. [PubMed: 23614898]
30. Anastassiadis T, Deacon SW, Devarajan K, Ma H, Peterson JR. Comprehensive assay of kinase catalytic activity reveals features of kinase inhibitor selectivity. Nat Biotechnol. 2011; 29:1039–1045. [PubMed: 22037377]

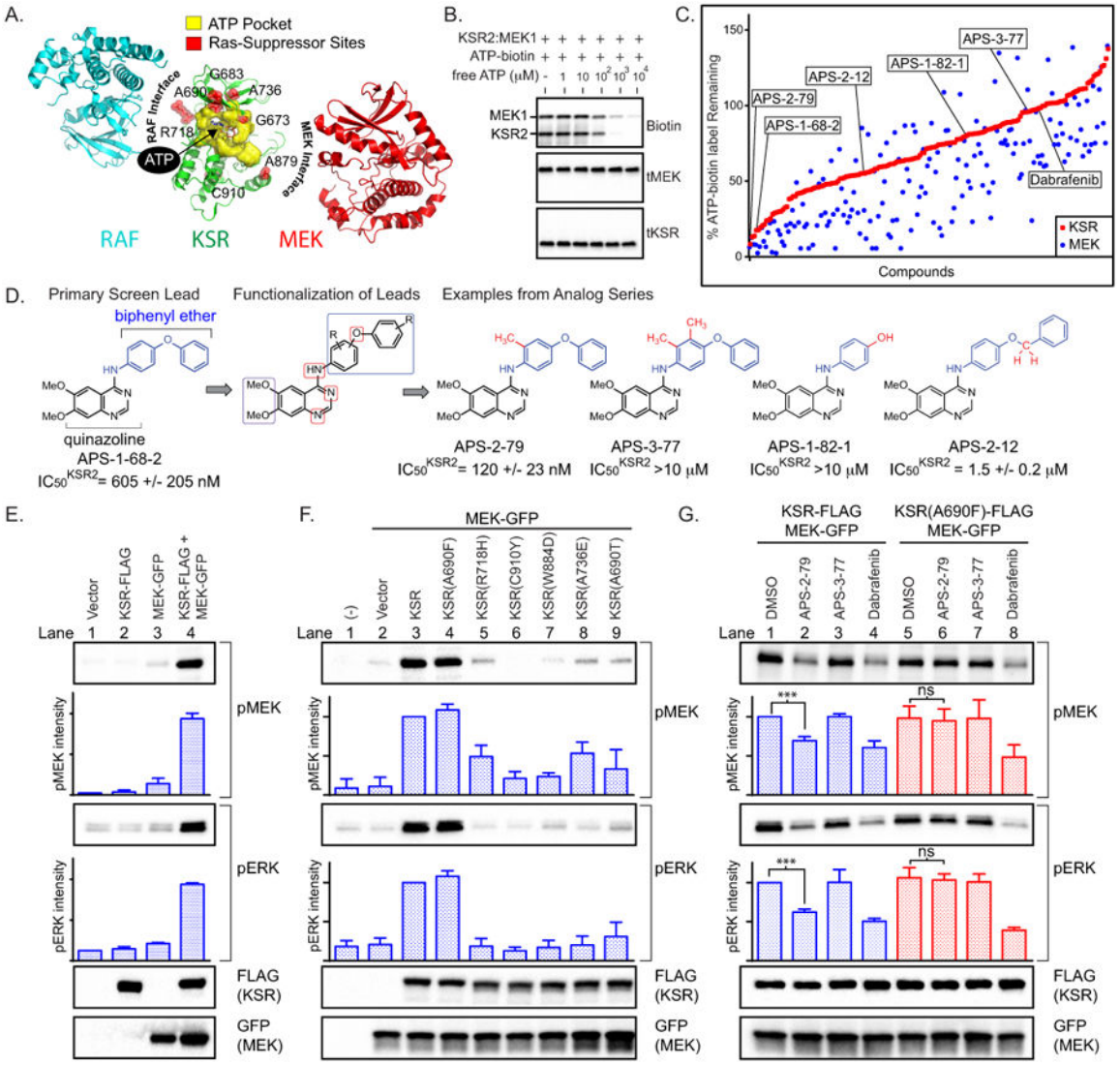

Figure 1. The small molecule APS-2-79 mimics KSR alleles that suppress oncogenic Ras mutations

a, Oncogenic Ras-suppressor mutations (red) localize to the ATP-binding pocket (yellow), as well as RAF- and MEK- interaction interfaces, in KSR. Shown is the putative structure of the RAF–KSR–MEK complex[7]. **b**, An activity-based probe (ATP^{biotin}) specifically labels the ATP-binding pockets of purified KSR2-MEK1 complexes. 2μM of ATP^{biotin} was incubated with KSR2–MEK1 in the presence of the indicated concentrations of free ATP. Biotin, total MEK, and total KSR western blots are shown. **c**, A kinase inhibitor screen for direct competitors of probe-labelling in purified KSR2–MEK1 complexes provides informative structure-activity relationships data. **d**, Chemical structures of leads. IC_{50} values (mean ± s.d.; $n = 2$ biological replicates) against ATP^{biotin} probe-labelling of KSR2 are listed below structures. **e**, Co-expression of full-length KSR–Flag and MEK1–GFP leads to enhanced MAPK signalling within 293H cells, as visualized by immunoblotting for phosphorylated MEK and ERK. **f**, MAPK activation is sensitive to known genetic suppressor mutations in KSR. A690F is a KSR mutant predicted to signal independent of

ATP-binding[16]. W884D is a loss-of-function mutation predicted based on structural analysis. Note, human KSR2 numbering used here and throughout. **g**, APS-2-79 impedes KSR-stimulated MAPK signalling within cells by wild-type KSR but not a control mutant (KSR(A690F)). Cells were treated with 5μM of APS-2-79, APS-3-77, or dabrafenib for 2 h. In **e**–**g**, cells were collected for western blot analysis 24 h after transfection. Error bars indicate the mean ± s.d. (n = 3 biological replicates). Signals were normalized relative to lane 1 (**e** and **g**) or 3 (**f**). NS, not significant. ***P < 0.0005 by two-tailed unpaired t-testing.

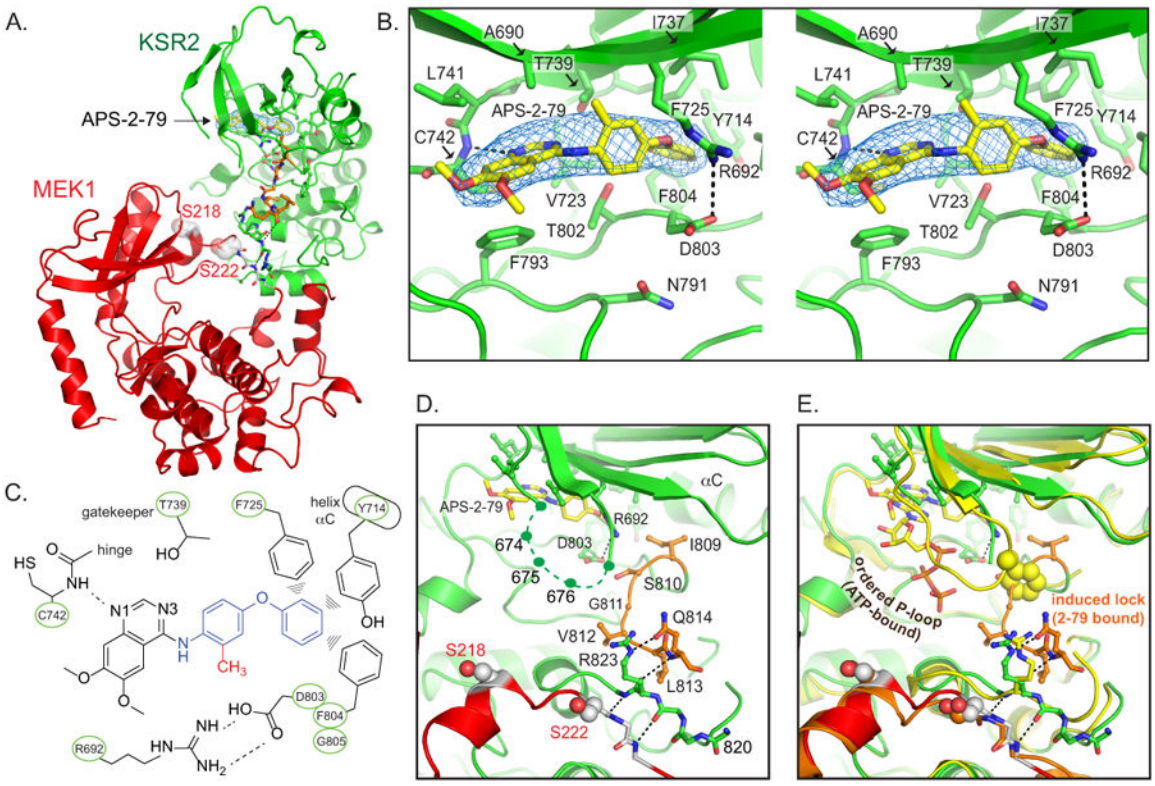

Figure 2. Structural analysis of APS-2-79 bound to the KSR2-MEK1 complex

a, The KSR2–MEK1–APS-2-79 complex. Highlighted are two key phospho-regulatory residues in MEK1, Ser218 and Ser222. **b**, Magnified stereo view of interactions between KSR2 and APS-2-79. $F_o - F_c$ omit map contoured at 3.5σ, generated with APS-2-79 omitted, is represented as a blue mesh. **c**, Schematic of the APS-2-79 binding site within KSR2. **d**, Magnified view of the KSR2 active site bound to APS-2-79, including the ‘induced lock (residues I809–Q814; orange). The disordered P-loop is highlighted by a dashed line. **e**, Overlay between the ATP-bound (yellow) and APS-2-79-bound states of KSR2.

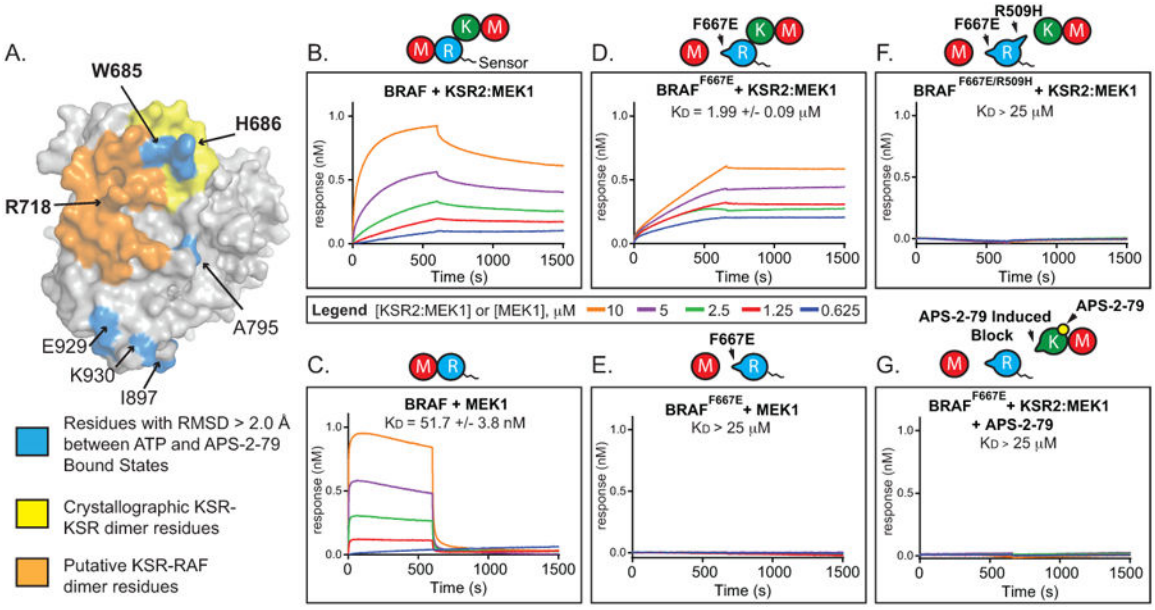

Figure 3. APS-2-79 impedes higher order assembly of RAF–KSR–MEK complexes

a, Mapping of residues with a root-mean-square (r.m.s.) deviation of >2.0 Å between the ATP- and APS-2-79-bound states of KSR2-MEK1 (blue) highlights alterations at contact residues Trp685 and His686 within the putative KSR–RAF heterodimer interface. **b**–**g**, BRAF and BRAF mutants (F667E and/or R509H) were immobilized on sensor-heads and KSR2–MEK1 or MEK1 assembly was monitored using bio-layer inferometry. Association occurred from 0 to 660 s and dissociation was monitored thereafter up to 1500 s. APS-2-79 was added in the presence of KSR2–MEK1 at a concentration of 25 μM. K_d values represent the mean ± s.e.m. derived from global fitting of all 5 binding curves.

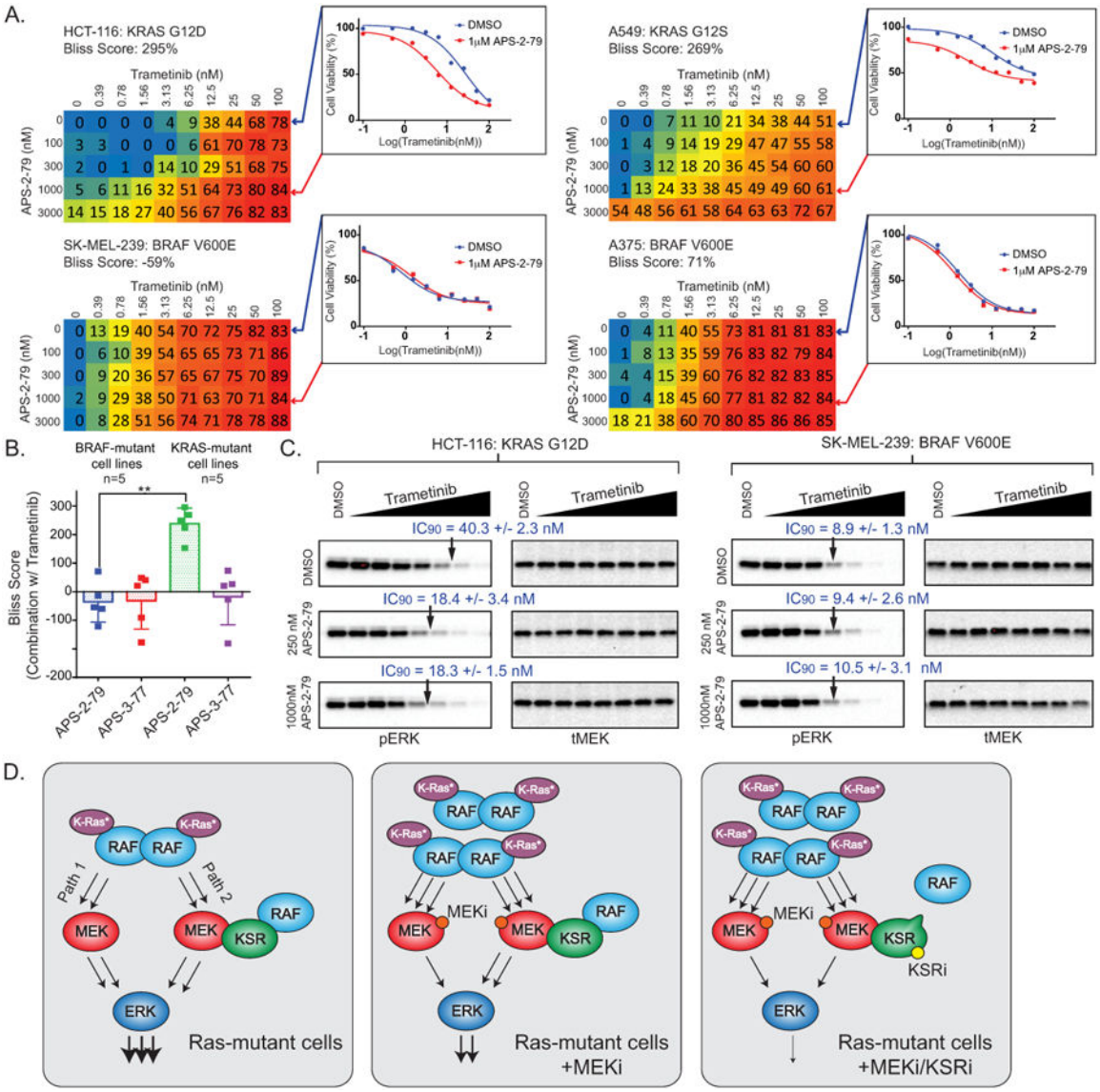

Figure 4. APS-2-79 Enhances the efficacy of the clinical MEK inhibitor trametinib within cancer cell lines containing K-Ras mutations

a, Dose–responses of APS-2-79 and trametinib (MEKi) on viability of K-Ras-mutant (HCT-116, A549) and BRAF-mutant (A375, SK-MEL-239) cell lines. Bliss scores represent the mean calculated from two biological replicates of the depicted concentration matrices. Numbers listed within synergy matrices, which represent the percentage of growth inhibition relative to DMSO controls, are the mean of the replicates. Insets highlight dose–responses of trametinib in the absence or presence of 1 μM APS-2-79 (points along each line represent the mean of two biological replicates). **b**, Synergy, as determined by Bliss independence scores (see Methods), for combinations of APS-2-79 and APS-3-77 with trametinib. Error bars represent the mean ±s.d. of Bliss scores as determined in **a** and Extended Data Fig. 9, derived from either K-Ras-mutant and BRAF-mutant cancer cell lines ($n = 5$ for each). $^{**}P < 0.005$ by two-tailed unpaired t-testing. **c**, Pathway analysis suggests that the increased potency of trametinib in the presence of APS-2-79 occurs through enhanced downregulation

of Ras-MAPK signalling (as measured by phospho-ERK). HCT-116 and SK-MEL-239 cells were treated for 48 h with increasing concentrations of trametinib combined with DMSO, 250 nM, and 1 μM APS-2-79. IC_{90} values represent the mean ± s.d. (n = 2 biological replicates). **d**, Model for synergy between the MEK inhibitor (MEKi) trametinib and the KSR inactive state binder (KSRi) APS-2-79. APS-2-79 enhances the efficacy of trametinib by antagonizing MEKi-induced Ras–MAPK signalling complexes.